IN-33
0610

NASA
Technical
Paper
3679

May 1997

Structural Design and Analysis of a Light-Weight Laminated Composite Heat Sink for Spaceflight PWBs

Mark S. Fan and W. Lee Niemeyer

**NASA
Technical
Paper
3679**

1997

Structural Design and Analysis of a Light-Weight Laminated Composite Heat Sink for Spaceflight PWBs

Mark S. Fan, Ph.D.
NASA Technology Validation Assurance Program
Greenbelt, Maryland

W. Lee Niemeyer
Goddard Space Flight Center
Greenbelt, Maryland

National Aeronautics and
Space Administration

Goddard Space Flight Center
Greenbelt, Maryland 20771

This publication is available from the NASA Center for AeroSpace Information,
800 Elkridge Landing Road, Linthicum Heights, MD 21090-2934, (301) 621-0390.

ACKNOWLEDGMENTS

The authors would like to express their gratitude to Ann Garrison-Darrin (GSFC code 310) for her generous support throughout the course of this work, and to Steve Waterbury (GSFC code 311) for the arrangement of additional computational power whenever needed. Thanks are also due to Jill Griffin (GSFC code 752), Gordon Casto (GSFC code 722) and Jay Parker (GSFC code 752) who provided many details in composite fabrication to us.

The authors are grateful to Dr. John LeNard (Litton Amecom Corporation) for the dynamic and thermal fatigue testing effort, and to Dr. E. Wong (Hughes Aircraft Company) for many useful discussions on LCC solder joint fatigue.

TABLE OF CONTENTS

LIST OF ILLUSTRATIONS

NOMENCLATURE

ASD	acceleration spectral density
CTE	coefficient of thermal expansion
D	plate flexural rigidity
E	Young's modulus
G	shear modulus, also gravitational constant
K	non-dimensional rotational spring stiffness
L_D	solder characteristic length
L_i	solder length
LCC	leadless chip carrier
N_f	number of cycle-to-failure
RMS	root-mean-square
T	absolute temperature
V	volume of finite element
W	plate deflection
a	plate lateral length
b	plate width
f	frequency of vibration
f(i)	i-th mode of PWB resonance (i = 1, 2, 3, ……)
h	plate thickness
ppm	parts per milliom
q	force loading

Greek Letters

$\Delta\gamma$	nonlinear shear strain range
α	coefficient of thermal expansion, also geometry related constant
β	rotational spring stiffness
ε	strain tensor
ε_{ii}	normal strain ($i = 1, 2, 3$)
γ_{ij}	shear strain ($i \leq j \leq 3$)
ν	thermal cycling frequency
ρ	density
σ	stress, also normal distribution parameter
υ	Poisson's ratio

Subscript

cemag	creep strain magnitude
s	symmetry

Superscript

C	cold extreme during thermal cycling
H	hot extreme during thermal cycling
cr	creep

STRUCTURAL DESIGN AND ANALYSIS OF A LIGHT-WEIGHT LAMINATED COMPOSITE HEAT SINK FOR SPACEFLIGHT PWBs

1. INTRODUCTION

Aluminum alloy plates are commonly used as heat sinks for many double-sided, high-density printed wiring board (PWB) assemblies in spaceflight applications. Sandwiched in between two circuit boards, they conduct the dissipated heat from electronic modules to mounted edges of the assembly. These plates also serve as a structural support providing necessary plane stiffness to the PWBs in order for the boards to survive the vibration environment during spacecraft launch and pyro-shock in orbit. With more and more payloads carried on each space mission, designing light-weight subsystems of the spacecraft becomes increasingly important. In electronic systems, bulk metallic materials are typically used for heat sinks, supports and enclosures. These metals constitute a large portion of the weight of the spaceborne systems, and replacing them by light-weight composite materials is proven to be very effective and reliable for weight improvement of future NASA spacecraft.

Another advantage of replacing the aluminum heat sink by the laminated composite is the reduction of thermal mismatch. During the pre-flight qualification testing, the PWB assembly is subject to thermal cycles with a minimum temperature range of 60 °C. Cyclic thermal stresses are induced within the layered structure of the board assembly and internal delamination could occur if thermal stresses are excessive. Since the mismatch between Kevlar board and aluminum heat sink is much higher than that between Kevlar and the laminate composite used, the thermally induced stresses are significantly reduced.

NASA Goddard Space Flight Center is currently designing PWB heat sinks and electronic enclosures with high-strength, light-weight composite materials for future spacecraft use. This report focuses on the PWB part, i.e., heat sink, board and electronic components, which is a working configuration to be used for NASA's MIDEX (Medium-Size Explorer) program.

2. BOARD CONFIGURATION

Figures 1-4 show the basic configuration of the double-sided board assembly. The thickness of the aluminum alloy heat sink (6061-T6) is 0.080 inch (Fig. 2). This alloy plate provides necessary plane stiffness to the whole board structure to meet the requirements of natural frequencies as well as dynamic responses, and has been used in several spacecraft in service. The weight of the plate can be estimated through the following calculation:

$$\begin{aligned}\text{Plate weight} &= \text{length}\times\text{width}\times\text{height (in}^3) \times \text{density (lb/in}^3) \\ &= abh\rho \\ &= (10.530\times7.528\times0.080)\times0.098 \\ &= 0.62 \ \ \text{lb} \qquad (2.1)\end{aligned}$$

When this plate is replaced by light-weight laminated composite material, the plane stiffness must remain more or less the same as that provided by the aluminum alloy plate in order to meet the dynamic requirements. This can be achieved by matching the fundamental frequency of the two heat sinks, i.e., aluminum plate and the composite, under the same boundary support conditions. Note that the lower density value typical for the composite material does not guarantee any weight reduction as the thickness of the composite heat sink will be different from 0.080 inch if the natural frequency is required to match in order to obtain the same plane stiffness. That composite thickness which satisfies the plane stiffness requirement will have to be determined during design process. This is a complicated issue because the laminated composite is not a uniform and isotropic material and therefore the thickness of the composite heat sink is not the only design variable. Multiple variables such as stacking sequence (total number of stacked composite laminates and orientation of each of them) will have to be incorporated into design. Since there are many ways of stacking up the composite laminates, choosing one that fits the best could be costly and time consuming if trial and error method is used. Through extensive parametric finite element modal analysis, many stacking scenarios were analyzed and the one that satisfies the dynamic requirements the most was identified within a short time period.

3. PWB AND ITS EDGE CONDITIONS

3.1 PWB Edge Constraints

Fig. 5 depicts the actual edge supports and constraints of the board assembly. In parametric finite element analysis (FEA), the multiple-pin edge connector was modeled as 100% fixity, both translational and rotational, along the length of the connector. However, modeling the commonly used 5-piece wedge lock requires more in-depth consideration.

It is well known that the multiple-piece wedge lock provides a fixity of the PWB edge somewhere between simple support and total fix. The value of the fixity depends on several variables such as number of pieces of the wedge lock and the torque of tightening the locking screws. For situations like this, regular displacement boundary constraints are invalid and spring elements with rotational stiffness must be introduced into the wedge locked edge of the PWB model. This rotational stiffness is directly related to the fixity of the wedge lock, and determination of the rotational stiffness is the key to accurate modeling of the wedge lock. This is an important step because the fixity of the board edge plays an essential role in dynamic responses of the PWB assembly.

3.2 PWB Vibration Modeling

In many applications, it is a common practice to model a PWB as a thin plate with appropriate boundary conditions. If a PWB lies in a x-y plane in a rectangular co-ordinates with its long edge parallel to x-axis, the governing equilibrium equation can be written as:

$$D\nabla^4 W(x,y,t) + \rho \frac{\partial^2 W(x,y,t)}{\partial t^2} = 0 \qquad (3.2.1)$$

where $\nabla^4 = \nabla^2\nabla^2$ and $\nabla^2 = \partial^2/\partial x^2 + \partial^2/\partial y^2$, $W(x,y,t)$ is plate transverse deflection, ρ is mass density per unit area, and D is plate flexural rigidity defined as:

$$D = \frac{Eh^3}{12(1-\upsilon^2)} \qquad (3.2.2)$$

h being thickness of the plate. The following boundary conditions shall apply to the plate edges (see Fig. 5):

Connector edge: $$W = \frac{\partial W}{\partial x} = 0 \qquad (3.2.3)$$

Free edge: $$\frac{\partial^2 W}{\partial x^2} + \upsilon \frac{\partial^2 W}{\partial y^2} = \frac{\partial^3 W}{\partial x^3} + (2-\upsilon)\frac{\partial^3 W}{\partial x \partial y^2} = 0 \qquad (3.2.4)$$

Lower wedge lock: $$\beta \frac{\partial W}{\partial y} - D\left(\frac{\partial^2 W}{\partial y^2} + \upsilon \frac{\partial^2 W}{\partial x^2}\right) = W = 0 \qquad (3.2.5)$$

Upper wedge lock: $$\beta \frac{\partial W}{\partial y} + D\left(\frac{\partial^2 W}{\partial y^2} + \upsilon \frac{\partial^2 W}{\partial x^2}\right) = W = 0 \qquad (3.2.6)$$

where β is rotational spring stiffness.

This set of equations governs the behavior of the PWB under the given edge constraints. Although obtaining analytical solutions through direct integration is not possible, several attempts were made using approximate methods such as Rayleigh-Ritz method and Galerkin method to solve for plate natural frequencies under different combination of the above boundary conditions [1-4].

3.3 Determination of Spring Rotational Stiffness

A combined theoretical-experimental method was used to determine the equivalent rotational stiffness provided by the 5-piece wedge lock used for the PWB assembly. To do that, another aluminum alloy plate (9.5"×7.528"×0.075") was used. That plate was constrained by two 5-piece wedge locks along its long edges and the first 3 natural frequencies were obtained through vibration test [5]:

f(1) = 222 Hz
f(2) = 270 Hz
f(3) = 423 Hz

To obtain the rotational stiffness of the springs, a FEA model of the same alloy plate was created with 800 shell elements. The material properties and boundary conditions used in the modeling are summarized in Table 1.

Table 1. Al Plate Properties and Boundary Conditions

Aluminum Alloy 6061 Properties	Young's Modulus (psi)	Poisson's Ratio	Density (lb/in^3)
	10×10^6	0.33	0.098
Connector Boundary Conditions	No Connector		
Wedge Lock Boundary Conditions	Dx=Dy=Dz=0, Rx=β, Ry=Rz=0		

where the units of β is lb/rad. These boundary conditions reflect the way the wedge locks mounted along the x-axis work; the 4th degree-of-freedom (DOF) is constrained somewhere between the simple support and total fix.

To establish the validity of the above wedge lock boundary conditions, several FEA runs extracting eigenvalues were performed. The results are listed in Table 2. It is shown that selection of β value has direct impact on the eigenvalue results, and using β for controlling the wedge lock fixity is indeed effective. The first 4 eigenmodes are shown in Fig. 6-9.

Table 2. Natural Frequencies under Various Edge Constraints

Wedge Lock Boundary Conditions	First 4 Natural Frequencies (Hz)
Simple Support	f(1) = 123.45 f(2) = 178.42 f(3) = 351.03 f(4) = 502.11
Total Fix	f(1) = 284.95 f(2) = 318.44 f(3) = 452.86 f(4) = 735.38
$\beta = 0.0001$	f(1) = 123.45 f(2) = 178.51 f(3) = 351.20 f(4) = 502.12
$\beta = 10^8$	f(1) = 284.94 f(2) = 318.43 f(3) = 452.85 f(4) = 735.38

For this purpose introduce a non-dimensional rotational spring stiffness *K*:

$$K = \beta (a/D) \tag{3.3.1}$$

where *a* is the plate lateral length. For this aluminum alloy plate, *D* is calculated to be 394.52 in-lb.

In a vibration restraint of wedge lock study, Barker *et al.* [6] concluded that wedge lock restraint is approximately proportional to the tightening torque of PWB mounting. For a 5-piece wedge lock, the non-dimensional rotational stiffness *K* was found to be nearly a constant ($K \sim 5$) when tightening torque is set at the manufacturer's suggested value (6 in-lb). The *K* value does not change even when the same wedge lock was used for other PWBs with different size and thickness. In their work, fundamental resonance was analyzed and measured.

A series of FEA runs were conducted with different *K* values to compare with natural frequencies from the test. Detailed results are given in Table 3. It is shown that frequency difference between $K = 4$ and $K = 5$ is slightly larger than 3% for the fundamental mode, less than 3% for the 2nd mode and less than 2% for the 3rd mode. For the fundamental mode, $K = 4$ matches the testing result almost exactly (222 Hz). Thus $K = 4$ is considered the best value for modeling this 5-piece wedge lock. Despite this good match, discrepancies are getting larger for higher modes.

Table 3. Impact of *K* Values on Natural Frequencies

$\beta = KD/a$ (lb/rad)		Natural Frequencies from FEA (Hz)
$K = 3$	$\beta = 124.5$	f(1) = 212.0 f(2) = 250.8 f(3) = 396.2
$K = 4$	$\beta = 166.1$	f(1) = 222.9 f(2) = 260.5 f(3) = 403.4
$K = 5$	$\beta = 207.6$	f(1) = 230.9 f(2) = 267.7 f(3) = 408.9

It should be remarked, however, that $K = 4$ does not predict higher frequencies well. The higher the vibrational modes, the larger the discrepancies (see Table 4).

Table 4. Natural Frequency Comparison

Vibrational Modes	1	2	3
Frequency (Hz) (FEA, K = 4)	222.9	260.5	403.4
Frequency (Hz) (Test)	222	270	423
FEA Errors (%)	0.41%	3.5%	4.6%

This phenomenon may be explained by looking at the modal shapes (Fig. 6-9). Higher modes are far more complicated and the motions are more rotational and non-uniform along the wedge locked board edges. It is suggested that using a universal *K* value for all the modes is incorrect. Because the motion complexity increases when the modes are getting higher, a *K* value good for the lower modes may not be good for even higher modes. In that sense, the *K* value is at best universal only for the fundamental mode.

4. NATURAL FREQUENCY FOR THE LAMINATED COMPOSITE HEAT SINK

4.1 Stacking Sequence Selection

With *K* value determined for the wedge lock, it is now possible to model the laminated composite heat sink. The composite candidate chosen was graphite/cyanate ester laminates based on P120/954-3. As mentioned earlier, many laminate stacking scenarios were analyzed with parametric FEA to compare with fundamental resonance of the aluminum heat sink. The final stacking sequence selected for the PWB assembly was $[(0\pm60)_2]_s$ with a total thickness of 0.070 inch (Fig. 10), which was found to be optimal. In fact, the fundamental frequency of this stacking sequence is slightly higher than that of the aluminum plate as a design improvement.

4.2 Determining Flexural Rigidity for Composite Stacking

For a given stacking sequence, plate flexural rigidity D must be determined in order to obtain the rotational stiffness of springs. Due to laminating in different orientations, the heat sink material is not homogeneous and Eqn. 3.2.2 cannot be directly used for calculating D. Thus the following semi-theoretical method was developed to obtain D for laminate composite.

For a rectangular plate with two opposite edges simply supported and the other two edges fixed, the maximum transverse deflection at the center of the plate under a uniform load has been mathematically solved [7]. The result is:

$$W_{max} = \alpha q b^4 / D \qquad (4.2.1)$$

where α is a geometry related constant, q is a uniformly distributed load, b is the length of the shorter edge of the plate and D is flexural rigidity. If maximum transverse deflection W_{max} is obtained using static FEA for the composite heat sink, flexural rigidity can be calculated by Eqn. 4.2.1. The aspect ratio (a/b) in this case is 1.398, thus the closest value of α is 0.0024 [7].

A FEA model of the composite heat sink with 875 shell elements per layer (a total of 16 layers based on Fig. 10) was created for modeling W_{max}. A static load of 10.0 lb was applied uniformly on the bottom side of the plate. Simply supported and totally fixed boundary conditions were applied to the model based on the analysis in [7]. The material properties used in this model are listed in Table 5.

Fig. 11 and 12 show the displacement and contour lines respectively. Under a uniform 10.0 lb load, the maximum center deflection is 0.00236 in. According to Eqn. 4.2.1, D equals 411.9 in-lb. Hence

$$\beta = KD/a = 156.4 \ \text{(lb/rad)} \qquad (4.2.2)$$

With this rotational stiffness, a finite element eigenvalue extraction yielded 273.8 Hz as the fundamental frequency for this stacking sequence. It is about 3% higher than the testing result (267 Hz) with a random input.

It is worth noting that, for a given stacking sequence, the plane stiffness can be increased or decreased by switching the [0°] and [90°] orientation of the fiber (see Fig. 13). This method was used in several earlier stacking selections in order to adjust the stiffness while keeping the same sequence. When this is used, E_{11} and E_{22} need to be interchanged, and ν_{21} should be obtained by:

$$\upsilon_{21} = \frac{E_{22}}{E_{11}} \upsilon_{12} \tag{4.2.3}$$

For stacking sequence $[(0 \pm 60)_2]_s$ used in this design, it was not necessary to adjust the composite plane stiffness, i.e., [0°] is defined as fiber orientation along the longitudinal direction of the board, based on the stiffness comparison with the alloy plate. In fact, this orientation switch for sequence $[(0 \pm 60)_2]_s$ yielded a nearly 30% higher fundamental frequency.

5. NATURAL FREQUENCIES FOR PWB ASSEMBLIES

Fig. 14a and 14b show the two PWB layer structures used for the analysis and testing. The first design uses a silicone rubber based compliant adhesive in order to "decouple" thermal expansion mismatch between heat sink and two Kevlar/Epoxy boards. The second one uses a rigid adhesive to attach the boards to heat sink for good bonding durability.

Another board assembly (shown in Fig. 2) is a baseline structure using aluminum alloy heat sink bonded with the compliant adhesive. This baseline assembly has a successful service record and the analysis and testing performed on it will be compared to its composite counterparts.

Generally an accurate dynamic modeling of a board assembly shall include all the details, i.e., all board layers, electronic components, I/O leads, solder joints, etc. While it is not impossible to do for a sparsely populated single-sided board assembly, it is just economically prohibitive for the current design. There are several ways to simplify the modeling effort, but each has its drawbacks [8]. The following lists frequently used methods:

A. Bare board only (no components included)
B. Global mass smearing
C. Global mass/stiffness smearing
D. Local smearing
E. Substructuring

Method A is the simplest, in which all electronic components are ignored. This weight reduction will artificially cause the natural frequency to increase. For a densely populated double-sided PWB, this ignored weight could amount to a large percentage of the total actual weight. However, Barker *et al.* [6] stated that, for normal electronic components, the drop in natural frequency due to added mass of mounted components is compensated for by the increase in natural frequency due to local increase in board stiffness from component mounting. This simple method is still considered useful in many applications when a detailed modeling is not practical.

Global mass smearing technique accounts for the total component masses by introducing an effective density for the entire PWB. This effective density is obtained by dividing the total mass of the PWB, including all components, by the volume of unpopulated PWB. Although actual mass on the board is considered in this approach, local stiffness increase due to component mounting is completely ignored. Hence there is no mass-stiffness compensation mentioned above, and accuracy of this method is in question.

Global mass/stiffness smearing adds the global stiffness effect due to components mounting to the global mass smearing, and is considered a good improvement compared to global mass smearing. However, to effectively utilize this technique, a force-displacement (bending and torsion) test must be performed to obtain the required stiffness of the board.

A natural extension to the above techniques is local smearing, in which stiffness variation due to local component mounting is experimentally determined and incorporated into the FEA model. This method requires more involved force-displacement testing.

Substructuring method is very effective when dealing with a system that has very large DOF. It divides the whole model into many smaller structures that are to be modeled independently, and DOF on the interface of each substructure is matched with the rest of the model. Since more than 50 surface mount components are mounted on both sides of the PWB assembly under study, using this technique is very time consuming.

Based on the above assessments, it was decided to model this board assembly using the simple method without including electronic components as first order approximation. Frequency results from testing are considered more appropriate and accurate, and shall be used whenever it is needed. All the material data used in modeling are given in Table 5.

Table 5. Material Properties for FEA

Materials	*E* (Msi)	*G* (Msi)	ν	ρ (lb/in^3)	*CTE* (ppm/°C)
Composite	E_{11}=68.24 E_{22}=0.70	G_{12}=0.74	0.321	0.06	α_{11}= -0.41 α_{22}= 25.0
Silicone Adhesive	0.000330	0.000127	0.3	0.053	200
Rigid Adhesive	0.32	0.122	0.33	0.031	74.2
Kevlar/Epoxy	4.5	-	0.28	0.071	6.8
EA Adhesive	0.30	-	0.29	0.041	70.7
63:37 Solder	4.32	-	0.4	0.305	24.7
Alumina	54	-	0.25	0.143	7.4
Aluminum Alloy	10	-	0.33	0.098	23.6

1. Composite data are from in-house testing by NASA GSFC [9].
2. Solder data in Table 5 are for room temperature only.

To obtain eigenmodes and frequencies of the PWB assemblies, two FEA models were constructed. Table 6 shows some details of the models.

Table 6. Details of FEA Models

FEA Models	Model 1 (Scenario I)	Model 1 (Scenario II)	Model 2
Model Structure	Laminate Composite	Laminate Composite	Laminate
Element Type	Shell	Shell	Shell
Heat Sink Type	Composite	Composite	Aluminum Alloy
Adhesive Type	Compliant	Rigid	Compliant
Adhesive Thickness (inch)	0.014	0.010	0.014

Once again, the semi-theoretical method for obtaining plate flexural rigidity *D* must be applied to each case by conducting a static loading FEA in order to determine the rotational spring stiffness. These results are listed in Table 7.

Table 7. Flexural Rigidity for Different Models

PWB Model	*K*	*D* (in-lb)	*β*=*KD*/*a* (lb/rad)
Aluminum Heat Sink	4	242.9	92.2
Composite (Silicone)	4	231.4	87.9
Composite (Rigid)	4	1314.7	499.4

Using rotational stiffness data listed in Table 7, FEA was conducted and fundamental frequency results are presented in Table 8. Also first four eigenmodes are plotted in Fig. 15-18.

Table 8. Fundamental Frequencies for the PWB Assemblies

	Fundamental Frequency (Hz)	FEA Errors (%)
Aluminum (Silicone) FEA	172.8	19.6
Aluminum (Silicone) Test	215.0	N/A
Composite (Silicone) FEA	166.2	19.9
Composite (Silicone) Test	207.5	N/A
Composite (Rigid) FEA	411.3	11.9
Composite (Rigid) Test	367.5	N/A

It is quite interesting to examine the above results. First of all, the simple method without modeling any mounted components seems acceptable as the first order approximation. For the complete PWB assembly with rigid adhesive used for heat sink attachment, total weight (in grams) is 699.3, 232.0 of which is the weight of 52 surface mount components. Ignoring all components means almost exactly a one-third weight reduction for the model (32.2% weight reduction for using silicone-based adhesive). The above FEA conclusions support the argument that frequency increase due to a large percentage of weight reduction is compensated for by frequency drop caused by local stiffness reduction from removing components. FEA errors could otherwise be a lot more significant. Secondly, several FEA test runs with a simple 1-sided PWB model indicated that this weight-stiffness compensation is generally less than 100% – meaning that natural frequency obtained from the simple method is usually higher than that from the full model which includes components mounting. The modeling result for the case of using rigid adhesive confirms that conclusion. For both cases with silicone-based compliant adhesive, however, frequency results are just the opposite. The predicted resonant frequency is about 20% lower than the testing value. A possible explanation is that, due to its very compliant nature, mechanical properties of the silicone-based adhesive are highly nonlinear compared to rigid adhesive, the properties of which are quite elastic. Since elastic properties were used for both analyses, it was expected that the results for rigid adhesive case are more accurate than that for silicone adhesive, which is indeed reflected in Table 8. Thus an in-depth characterization of the hyper-elastic behavior of the silicone adhesive is required for future projects using this material.

6. RANDOM VIBRATION ANALYSIS

Finite element random vibration and dynamic response analyses were performed for all three PWB configurations under the same boundary constraints in order to obtain the largest board deflections at the fundamental resonance. The input acceleration spectral density (ASD), required for spacecraft subsystems during pre-flight qualification testing, is shown in Table 9 (also in Fig. 19).

Table 9. Acceleration Spectral Density

Frequency (Hz)	Acceleration (G^2/Hz)
20	0.0016
20 - 80	6 dB/oct
80-1000	0.16
1000-1200	-8 dB/oct
1200-2000	0.0016
Overall G_{rms}	11.3

For all three cases, this ASD was applied to the direction perpendicular to the board plane (Z-axis) and a 10% damping factor was used in the analysis. Table 10 summarizes the FEA random vibration results.

Table 10. PWB Deflections under Random Vibration Conditions

PWBs Design	Composite (Silicone)	Composite (Rigid)	Aluminum (Silicone)
Max. Center Deflection (3σ RMS) at First Resonance (inch)	0.033	0.0075	0.031
Max. Free-Edge Deflection (3σ RMS) at First Resonance (inch)	0.066	0.0162	0.065
Max. Free-Edge Deflection / PWB-Thickness Ratio	0.27	0.07	0.26

As shown in the table, stiffness of the PWB with composite heat sink and compliant adhesive is indeed very similar to that of the aluminum heat sink with the same adhesive. However, using rigid adhesive for attaching composite heat sink makes the PWB much more stiff.

7. THERMAL CONSIDERATIONS

It has been demonstrated that replacing metallic alloy with laminate composite as heat sink material is promising for the current design in terms of reducing weight and maintaining required stiffness. However, the ultimate purpose of designing a proper heat sink is to effectively conduct the heat dissipated from electronic modules mounted on both sides of the assembly. For steady-state power dissipation, there is only one single parameter governing the heat conduction capability: thermal conductivity of the heat sink material. The higher the conductivity, the better the heat sinking. The in-plane thermal conductivity is 167 W/m°C for aluminum alloy (6061-T6), and 168 W/m°C for the composite with $[(0\pm60)_2]_s$ stacking sequence. Apparently the heat conduction capability for both heat sink materials is almost identical in the in-plane directions which are the main paths of heat transfer. Note that conductivity of the composite through the board thickness is about an order of magnitude lower compared to its in-plane component.

Another important issue is thermal mismatch. It is related to the coefficient of thermal expansion (CTE) of adjacent materials structurally attached together. Because of the thin aluminum sheets (0.002 inch) and the EA adhesive used in composite heat sink design, an intuitive thermal mismatch comparison to the aluminum heat sink assembly is not conclusive. For the PWB with composite heat sink and silicone-based adhesive, induced thermal stress due to temperature cycling is nearly negligible because of the adhesive compliance. For the case with rigid adhesive, the in-plane shear stress distribution in the layer of the adhesive itself shall be examined under cyclic temperature loadings because of its rigidity.

A thermal stress analysis was conducted for the design with composite sink and rigid adhesive under a cyclic thermal condition from 0 °C to 100 °C (see Table 5 for CTE properties). The maximum shear stress distribution in the rigid adhesive at 100 °C is shown in Fig. 20. The highest stress, occurred around the end of both wedge locks on the free-edge side, is about 104 psi, compared to its shear strength (5770 psi) and ultimate shear strength (5930 psi). This indicates that, under such a thermal cycling, rigid adhesive bonding for the composite heat sink is structurally stable. As a direct comparison, the same analysis was performed by replacing the composite heat sink with the 0.080" thick aluminum alloy heat sink. For the latter case, the maximum shear stress occurred in the same area in the adhesive layer is 655.6 psi, almost 6 times higher.
It is quite clear that using composite heat sink to reduce inner-layer thermal stresses is effective.

8. SURFACE MOUNT SOLDER JOINT FATIGUE ANALYSIS

It is well established that low-cycle thermal fatigue is the major failure mechanism for surface mount solder joints. Understanding the life expectancy of the solder joints under a given thermal environment is of critical importance, especially for spaceflight applications where a typical service life is expected to last for years and replacing failed electronic subsystems is cost prohibitive or perhaps virtually impossible. This reality makes solder joint integrity a critical issue in quality assurance and reliability efforts for spaceborne electronic systems.

Surface mount solder joint fatigue failure has been a central topic of study in recent years because of its criticality and frequent occurrence. Large amount of data have been generated through theoretical, experimental and numerical modeling methods. However, most of the studies focus on compliant solder joints such as gull-wing and J-lead, and very few are dealing with stiff solder joints, leadless chip carrier (LCC) solder joint being a typical category. Generally stiff joints are more susceptible to low-cycle fatigue damage compared to joints with sufficient compliance. Therefore it is necessary to seek a better understanding of fatigue behavior of stiff solder joints. To date there are very few comprehensive LCC solder joint fatigue/creep studies published in the literature, presumably due to its low popularity in commercial electronic products.

In the current PWB assembly design, the majority of devices are LCCs mounted on both sides of the Kevlar/Epoxy board. Several different types of LCCs are used and their major differences are the dimensions and I/O counts. Of particular interest in solder reliability analysis is thermal fatigue damage behavior of the worst-case joint, which should be one of the corner joints of the largest LCC component on board. This largest LCC was identified as the 84-joint ceramic (Alumina) device, the dimensions of which follow nominal JEDEC (Joint Electron Device Engineering Council) registration.

In theory, a simultaneous thermal/structural FEA can be performed for the complete PWB assembly including all the devices and solder joints. However, it is computationally too expensive. In this study, a device-level approach was taken, i.e., modeling the largest LCC emphasizing stress and fatigue/creep behavior of one corner joint. Due to symmetry, a one-quarter FEA model for this device was created (Fig. 21) for analysis. In order to reduce the degree-of-freedom in the model so that the computational time is acceptable with a high-performance workstation, bilinear multi-point constraint (MPC) was utilized in the interface between LCC solder joint and PWB surface. This model size reduction is very significant due to multiple-layer structure of PWB where finite element continuity needs to be maintained. Without MPC, the element density in every layer of PWB would have to be much higher, resulting in a model with more than twice the number of nodes. Note that in Fig. 21 only the first element layer of the Kevlar board is shown for clarity. Two symmetric boundary conditions were applied along the two planes of symmetry, and one node at the intersection of the symmetric planes was totally restrained to avoid rigid body motion.

8.1 Constitutive Model for Eutectic 63Sn:37Pb Solder

As mentioned above, low-cycle fatigue is usually the dominant cause of damage and failure of solder joints. Thus determining low-cycle fatigue properties of solder alloy is of great importance in solder joint reliability studies. At elevated temperatures (typically higher than one-half of the melting temperature), most solder alloys exhibit significant creep and stress relaxation behavior, which is responsible for so-called creep rupture along the alloy grain boundaries and therefore causing failures. Physically this high temperature behavior is characterized by large inelastic strains mainly consisting of time-independent plastic and time-dependent creep components. Creep strain is considered the most critical time-dependent damage accrual mechanism, and damaging effect from creep strain is the same as more immediately induced plastic strain. In a detailed analysis, creep strain must be summed with the plastic component to obtain the total inelastic strain which is correlated with solder joint fatigue life. Also, because of creep, the total strain range is a strong function of solder temperature. All these make the solder constitutive model highly nonlinear and complex.

Several constitutive models are available for solder alloys. In this work, a combined creep-rupture and plasticity model, proposed by Wong, Helling and Clark for 63Sn:37Pb eutectic alloy [10], was used in the analysis.

$$\frac{\partial \varepsilon}{\partial t} = \frac{1}{E}\frac{\partial \sigma}{\partial t} + B_1 D(\frac{\sigma}{E})^3 + B_2 D(\frac{\sigma}{E})^7 \qquad (8.1.1)$$

where

$\partial\varepsilon/\partial t$ = total strain rate
σ = stress in solder
E = Young's modulus
= $(5.6 \times 10^4 - 88T)$ (MPa)
D = exp(-5413/T)
T = absolute temperature (K)
B_1 = constant = 1.7×10^{12} (s^{-1})
B_2 = constant = 8.9×10^{24} (s^{-1})

Eqn. 8.1.1 has been implemented into ABAQUS (a commercial FEA code) by developing a user supplied material subroutine in which an implicit finite difference algorithm was utilized for discretization.

8.2 FEA Results

In the analysis, a cyclic thermal profile (Fig. 22) starting from room temperature (25 °C, also set as stress-free state) and ranging from -50 °C to 100 °C with a dwell time of 15 minutes was applied to the model which was the composite/silicone configuration. Initially all the solder joints were modeled according to Eqn. 8.1.1, however the first run failed due to out of hard disc space after more than a day of running time. This was expected because in a nonlinear analysis the system stiffness matrix is updated after every time increment, which is very CPU intensive. One possible way of solving this problem was to apply Eqn. 8.1.1 to only the two corner joints and use linear properties at room temperature for other joints. Since only the corner joint is of primary interest, this simplification may be reasonable. Nevertheless the impact of this simplification needs to be evaluated. Two test runs were performed to investigate the effect, one with Eqn. 8.1.1 applied to all the joints and the other to only the two corner joints. In order to carry out these runs with the existing workstation, only first 35 minutes of the temperature profile in Fig. 22 was used in both runs. Comparison of the results indicated that the peak difference of the maximum local von Mises stress in the corner joint at about 21st minute was 4.9%. Hence this method for significant run-time reduction was adopted in the subsequent computations in which a total of 4 joints, i.e., 2 corner ones and 2 adjacent ones, were in fact modeled based on Eqn. 8.1.1, and the others were assigned with linear properties.

Fig. 23 plots the maximum local von Mises stress in one of the corner joints. It shows a similar cyclic pattern with quite low stresses (< 4 MPa) at 100 °C plateaus and very high stresses (≈ 100 MPa) at -50 °C dwells. Due to its stiff characteristics, cyclic peak stress in a LCC corner joint under a nominal thermal loading can be several times higher than the solder yield strength. However, this extremely high stress does not hold in the solder joint. Rapid stress relaxation starts immediately after the peak stress is reached due to strong creep effect. During thermal cycling, considerable creep strain and creep strain energy are being accumulated in the solder joint. It is this accumulating strain field that causes the fatigue failure of the solder joint.

Time-dependent equivalent creep strain magnitude in the corner joint is shown in Fig. 24. This multi-axial strain field can be expressed as:

$$\varepsilon_{cemag} = \sqrt{\frac{2}{3}\varepsilon^{cr}:\varepsilon^{cr}} \tag{8.2.1}$$

where ε^{cr} is the creep strain tensor. It can be seen from the plot that the creep strain magnitude exhibits a slow and progressive upward drift behavior, compared to the plastic strain field in which a stable strain range can normally be defined. The drift illustrates the most important difference between isothermal mechanical cycling and thermal cycling, which stems from the strong temperature dependence of creep. This unique phenomenon can also be demonstrated by plotting shear stress vs. total strain in shear during thermal cycling (see Fig. 25). The direction of drift is moving toward the higher strain. It is a phenomenon understood only recently through nonlinear FEA simulations, and is referred to as "creep ratcheting" [11].

Because fatigue failure in solder occurs in an incremental accumulation fashion, the cumulative deformation is logically selected as a criterion for damage analysis [12]. Cumulative equivalent creep strain provides a way of estimating cumulative deformation in solder and was obtained through time integration of Eqn. 8.2.1. This cumulative method can also be applied to solder joints subject to other types of thermal exposure. In Fig. 26, cumulative equivalent creep strain is plotted as the function of time for the corner joint. Another way of estimating solder fatigue damage is to analyze strain energy accumulated in the joints [13]. Fig. 27 shows the total creep strain energy in the corner solder joint. Both equivalent creep strain and total creep strain energy demonstrate the monotone accumulative feature, which is virtually the intrinsic cause of fatigue damage failure in a solder joint.

An interesting comparison was made between the above model and an isolated corner joint model, i.e., all other solder joints except the corner one were removed from the model. The single joint model yielded a 36% higher creep strain energy, compared to 40% for a 52-pin J-lead surface mount device as reported by Bhatti, *et. al.* [14].

The above analyses were also performed on the other two PWB configurations, i.e., composite heat sink with rigid adhesive, and aluminum heat sink with silicone-based adhesive. These results have shown that, although dynamic characteristics changed significantly, as summarized in Tables 7 and 8, if different heat sink or adhesive materials were used, differences of the peak thermal stress in the corner solder joint was small. Compared to the composite/silicone configuration, the composite/rigid configuration has a 3.1% difference, and the one with aluminum heat sink has a 5.8% difference. These analytical conclusions indicate that thermal stresses in LCC solder joints are mainly induced by thermal mismatch between solder and Kevlar board, and the influence of thin-layer adhesive attaching Kevalr board to heat sink, whether rigid or compliant, is nearly negligible.

8.3 Cycle-to-Failure Analysis

As has been discussed above, the creep ratcheting phenomenon makes the creep strain range non-deterministic, therefore a simple method of strain summation from the stabilized hysteresis loop is in a strict sense not applicable. As an alternative, Wong [15] and Solomon [16] suggested an averaging method which can be expressed as follows:

$$N_f = 1.07 v^{0.32} (\Delta\gamma_{ne})^{\frac{-1.0}{0.46}} (\frac{L_i}{L_D}) \qquad (8.3.1)$$

where

v = temperature cycling frequency (Hz)
N_f = number of cycle-to-failure
$\Delta\gamma_{ne}$ = volumetric average of nonlinear shear strain range
L_i = length of solder joint
L_D = characteristic length, 0.0625 in < L_D < 0.25 in

In the following analysis, v was calculated, based on Fig. 22, to be 1.8×10^{-4} Hz, L_i was taken as 0.060 in., and L_D was selected as 0.25 in. for most conservative estimation.

Next step is to determine the averaged nonlinear shear strain range $\Delta\gamma_{ne}$ induced during one complete temperature cycle. This shear strain range is calculated based on the two temperature extremes, i.e., -50 °C and 100 °C. Using von Mises stress-strain relations, the nonlinear shear strain range for each solder element is:

$$\Delta\gamma_{nee} = \{2[(\varepsilon_{11}^H - \varepsilon_{11}^C)^2 + (\varepsilon_{22}^H - \varepsilon_{22}^C)^2 + (\varepsilon_{33}^H - \varepsilon_{33}^C)^2] + (\gamma_{12}^H - \gamma_{12}^C)^2 + (\gamma_{23}^H - \gamma_{23}^C)^2 + (\gamma_{13}^H - \gamma_{13}^C)^2\}^{\frac{1}{2}} \qquad (8.3.2)$$

where H and C denote hot and cold temperature dwells respectively. Note that these nonlinear strain values are taken at the end of hot or cold plateaus. Thus the volumetric average of the nonlinear shear strain range is:

$$\Delta\gamma_{ne} = \frac{\sum \Delta\gamma_{nee} V_e}{\sum V_e} \qquad (8.3.3)$$

where V_e is the volume of each 3-dimensional solid element in the corner solder joint. $\Delta\gamma_{ne}$ obtained from Eqn. 8.3.3 was used in Eqn. 8.3.1 to calculate the number of cycle-to-failure, N_f, which was found to be 110 cycles.

It should be noted that this cycle-to-failure result is not meant to be used as guidelines for pre-launch qualification testing mainly because the characteristic length, L_D, is unknown for LCC solder joints. The value range (0.0625 in < L_D < 0.25 in) suggested by Solomon was based on a specific testing specimen used in a lap shear test, which has a very different configuration compared to a typical LCC solder joint. Using 0.25 in. for conservative estimation could be totally misleading. In fact, a recent work by Wong and Cohen [17] on gull-wing solder joint durability suggested a L_D value as 0.01066 in., which is completely out of Solomon's range. This length for LCC joints is yet to be determined, and large amount of LCC cycle-to-failure fatigue testing data will be required to determine its value. Based on the application environment, this board assembly with composite heat sink was tested for 500 thermal cycles ranging from 0 °C to 100 °C, and no obvious solder defects were found after the testing.

9. CONCLUSIONS

NASA Goddard Space Flight Center has successfully demonstrated the application of laminated composite material as heat sink for double-sided high-density spaceflight PWB assemblies. This innovative approach allows a significant reduction in assembly weight and internal thermal stresses that are largely responsible for potential delamination. To save time and cost, a concurrent engineering approach was utilized and all the different design configurations were thoroughly analyzed, evaluated and compared before an optimized design was proposed. Through effective use of finite element analysis tools as well as numerous parametric what-if studies, the final design selected can achieve its maximum performance. Extensive testing efforts were also made to validate the modeling techniques and parameters.

Of particular importance in this work is the contribution to our understanding of creep behavior of LCC surface mount solder joints, which is critical for long-term reliability of solder connections, spaceborne electronic systems, and ultimately the spacecraft. Methodologies used in this work can readily be applied to many other applications associated with electronic components and assemblies.

Future research work in LCC solder joint needs to include determination of the characteristic length used in the analysis through extensive lab fatigue testing. This will produce a more accurate cycle-to-failure result.

REFERENCES

[1] Gorman, D. J., "A general solution for the free vibration of rectangular plates resting on uniform elastic edge supports," *J. Sound and Vibration*, Vol. 139(2), pp. 325-335, 1990.

[2] Leissa, A. W., "The free vibration of rectangular plates," *J. Sound and Vibration*, Vol. 31(3), pp. 257-293, 1973.

[3] Laura, P. A. A. and Grossi, R., "Transverse vibration of a rectangular plate elastically restrained against rotation along three edges and free on the fourth edge," *J. Sound and Vibration*, Vol. 59(3), pp. 355-368, 1978.

[4] Warburton, G. B. and Edney, S. L., "Vibrations of rectangular plates with elastically restrained edges," *J. Sound and Vibration*, Vol. 95(4), pp. 537-552, 1984.

[5] LeNard, J., *et al.*, "Thermal and vibration tests of composite heat sink electronic component assemblies," *Litton Amecom Rep. for NASA GSFC, AM149-0016(155),* Aug. 1996.

[6] Barker, D. and Chen, Y. S., "Modeling the vibration restraint of wedge lock card guides," *Proc. ASME Winter Annual Meeting*, pp. 1-7, Nov. 1992.

[7] Timoshenko, S. and Krieger, S. W., *"Theory of Plates and Shells,"* McGraw-Hill, 1959.

[8] Pitarresi, J. M. and Primavera, A. A., "Comparison of modeling techniques for the vibration analysis of printed circuit cards," *J. Electronic Packaging*, Vol. 114, pp. 378-383, 1992.

[9] Viens, M., "P-120 composite structural testing report," NASA GSFC Code 313, 1996.

[10] Wong, E., Helling, D. E. and Clark, R. W., "A creep-rupture model for two-phase eutectic solders," *IEEE Trans. on Comp., Hybrids, and Manufacturing Tech.,* Vol. 11, No. 3, pp. 284-290, 1988.

[11] Ross, R. G. Jr. And Wen, L. C., "Solder creep-fatigue interactions with flexible leaded surface mount components," in *Thermal Stress and Strain in Microelectronics Packaging*, Ed. J. H. Lau, pp. 607-647, Van Nostrand Reinhold, 1993.

[12] Pan, T. Y., "Thermal cycling induced plastic deformation in solder joints - Part I: Accumulated deformation in surface mount joints," *J. Electronic Packaging*, Vol. 113, pp. 8-15, 1991.

[13] Pan, T. Y., "Thermal cycling induced plastic deformation in solder joints - Part III: Strain-energy based fatigue life model and effects of ramp rate and hold time," *Proc. ASME Winter Annual Meeting,* Dec. 1991.

[14] Bhatti, P. *et. al.*, "Three-dimensional creep analysis of solder joints in surface mount devices," *J. Electronic Packaging*, Vol. 117, pp. 20-25, 1995.

[15] Wong, E., Personal communications, 1996.

[16] Solomon, H. D. *et al.*, "Predictions of solder joint fatigue life," *Proc. 40th IEEE ECTC*, pp. 351-359, 1990.

[17] Wong, E. and Cohen, H. M., "Gull-wing solder joint durability evaluation," to be published, 1996.

LIST OF ILLUSTRATIONS

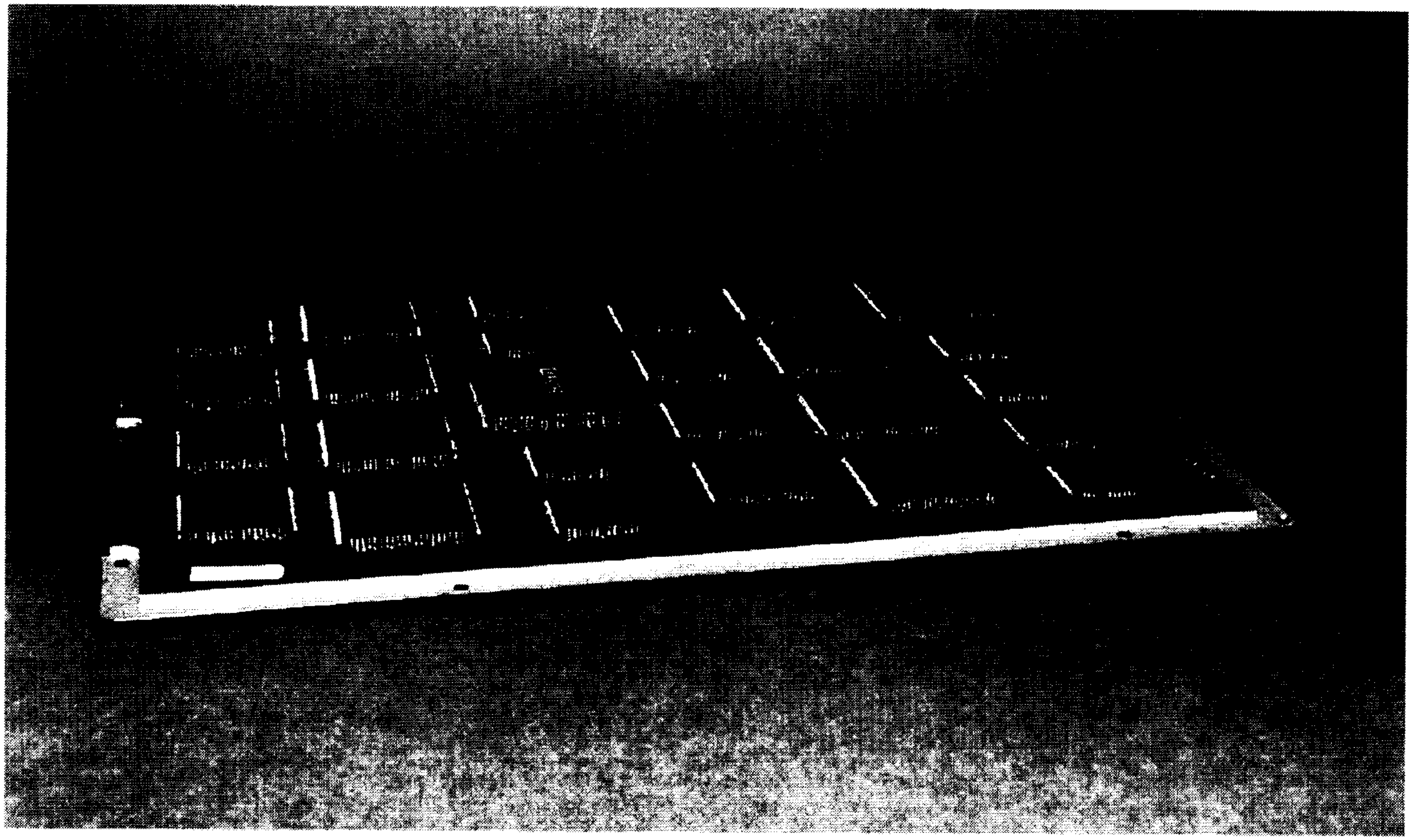

Figure 1. Prototype PWB assembly with composite heat sink.

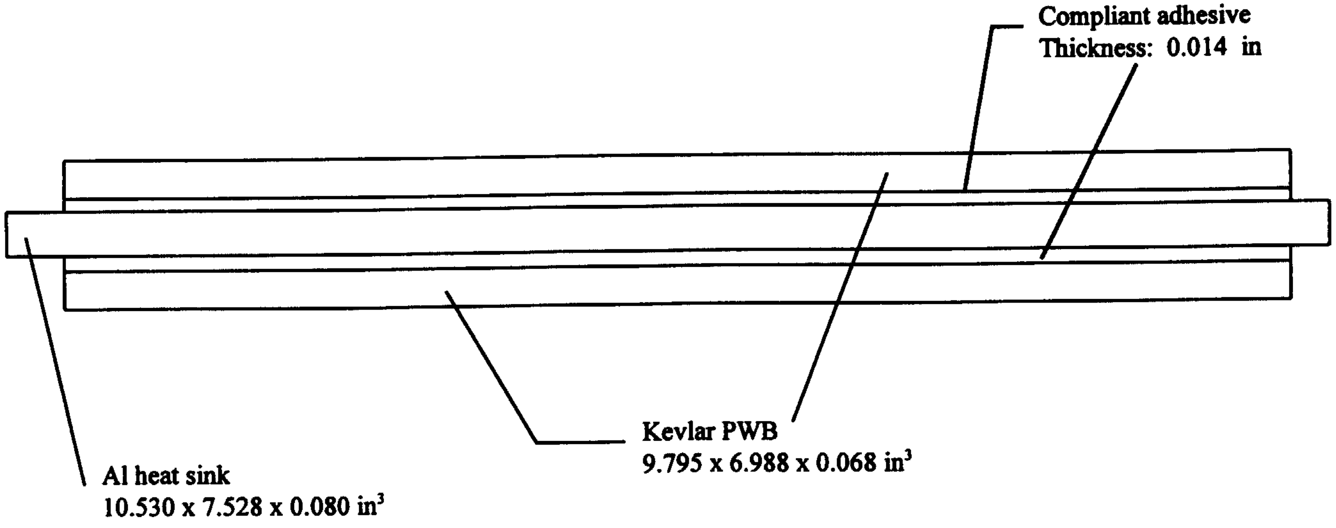

Figure 2. Side-view of the baseline PWB assembly with Al heat sink (not to scale).

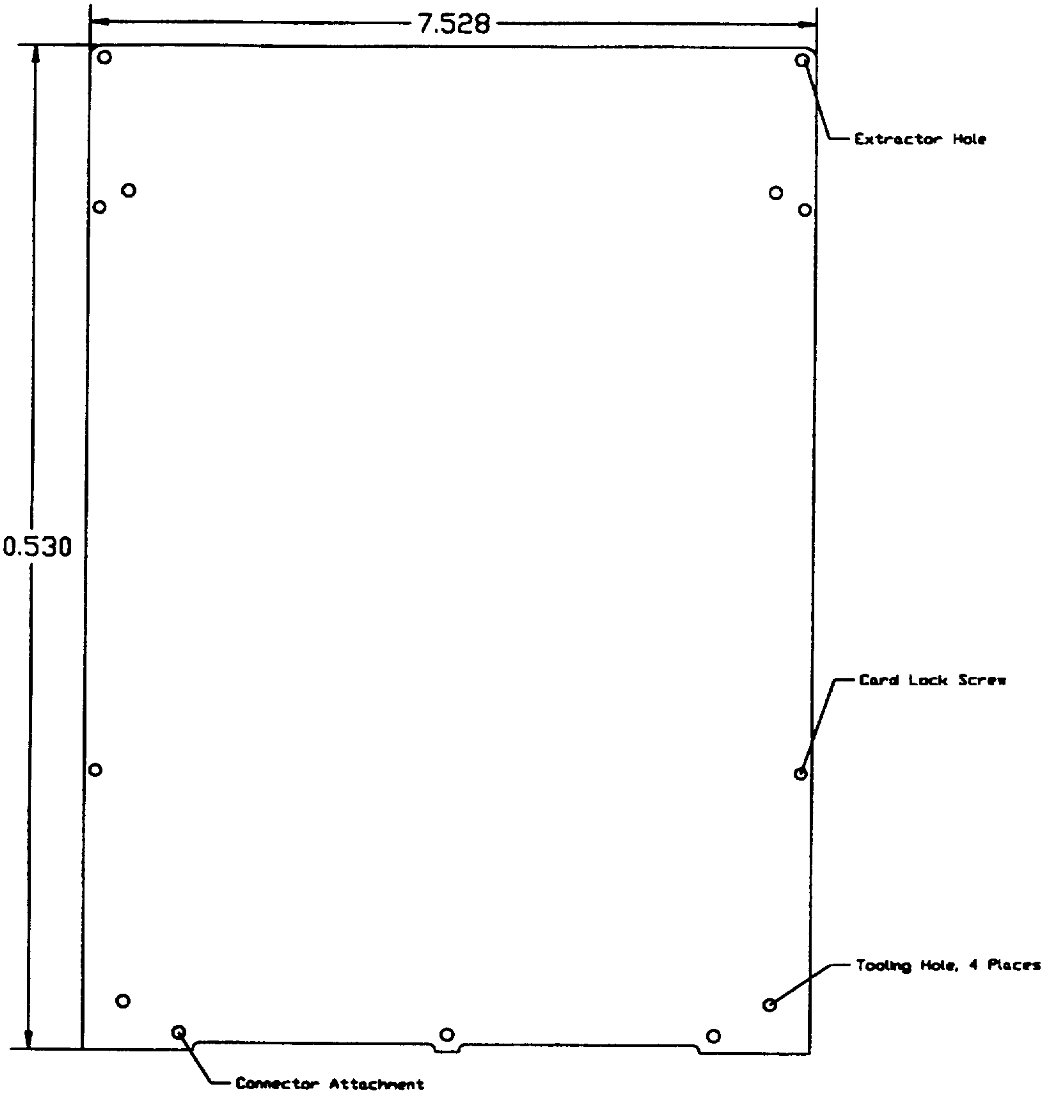

Figure 3. Heat sink outline.

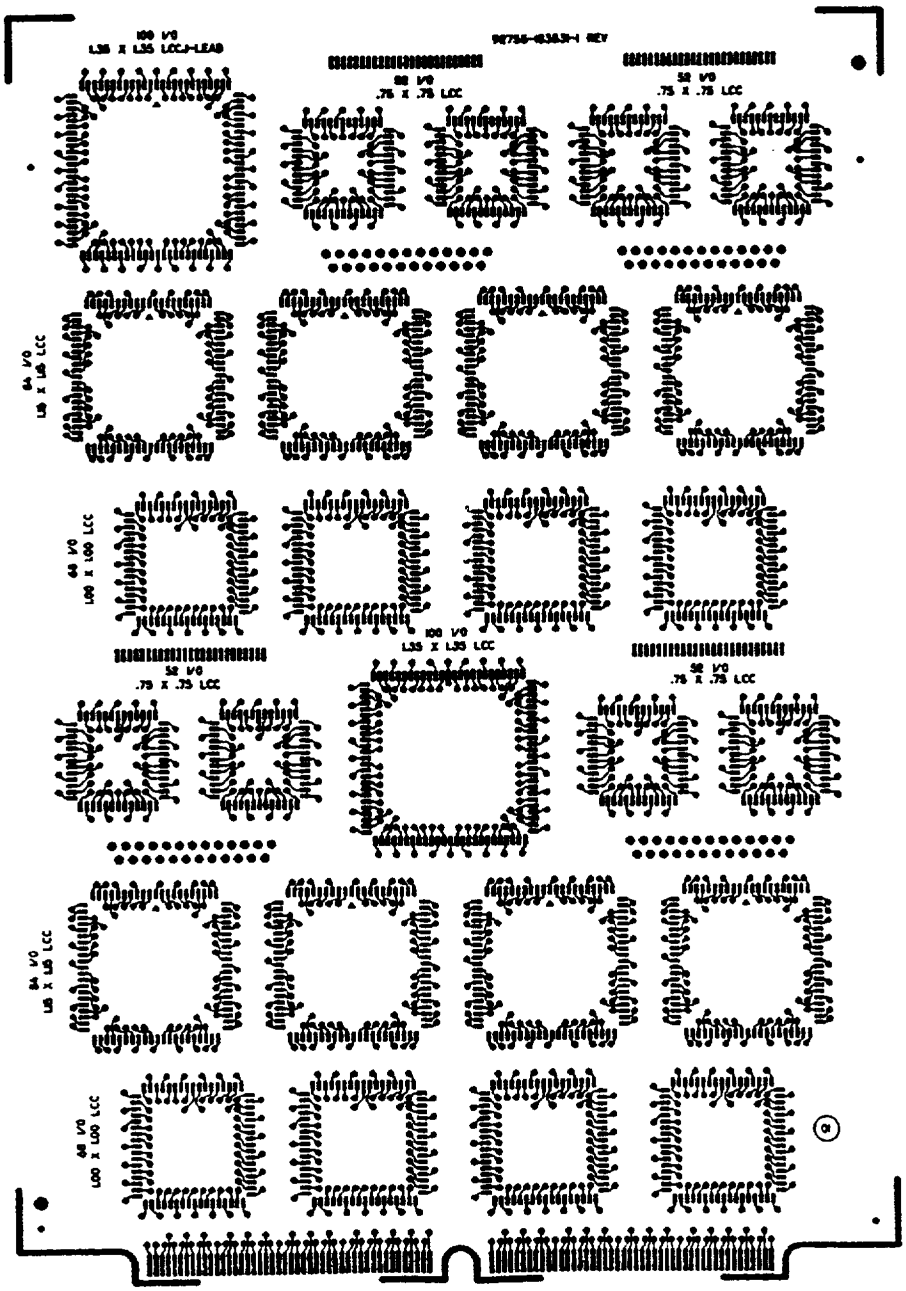

Figure 4. PWB layout.

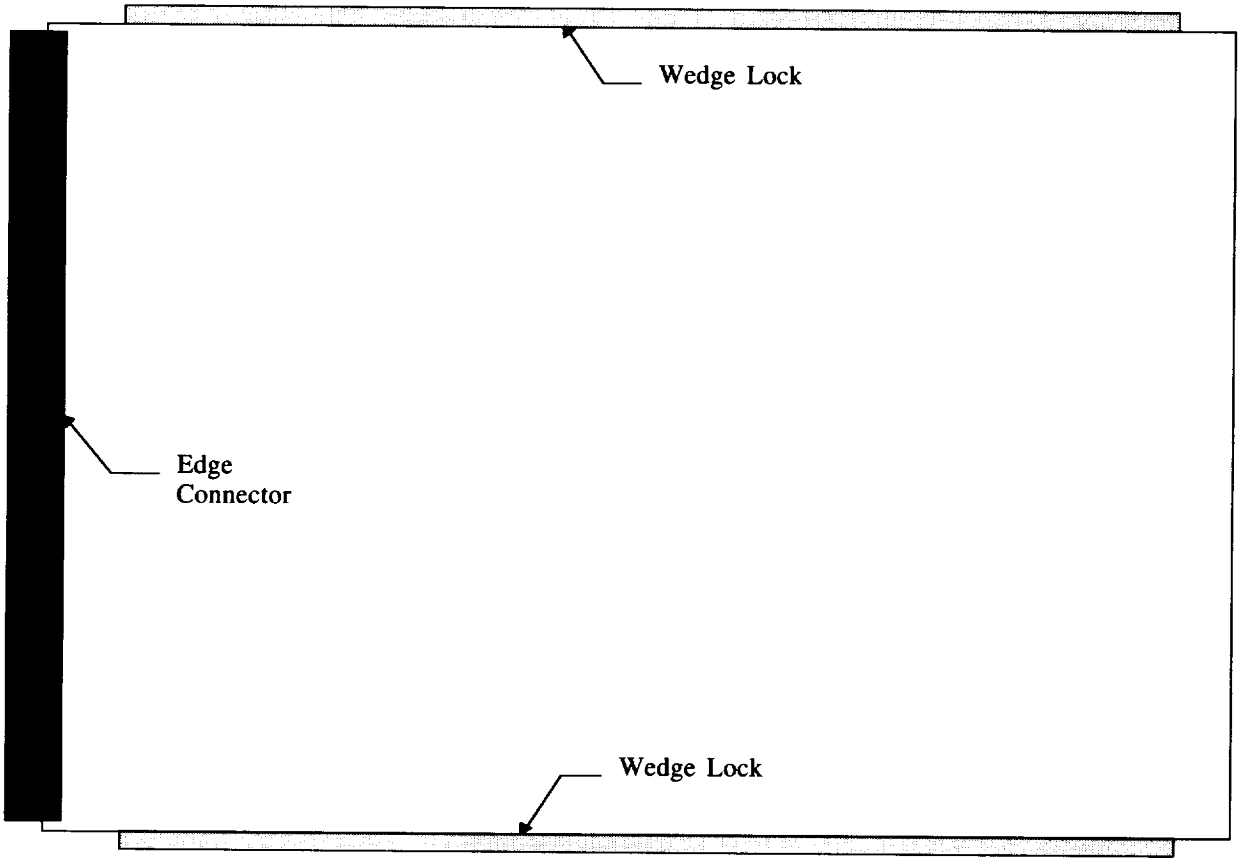

Figure 5. Edge supports for the PWB assembly (not to scale).

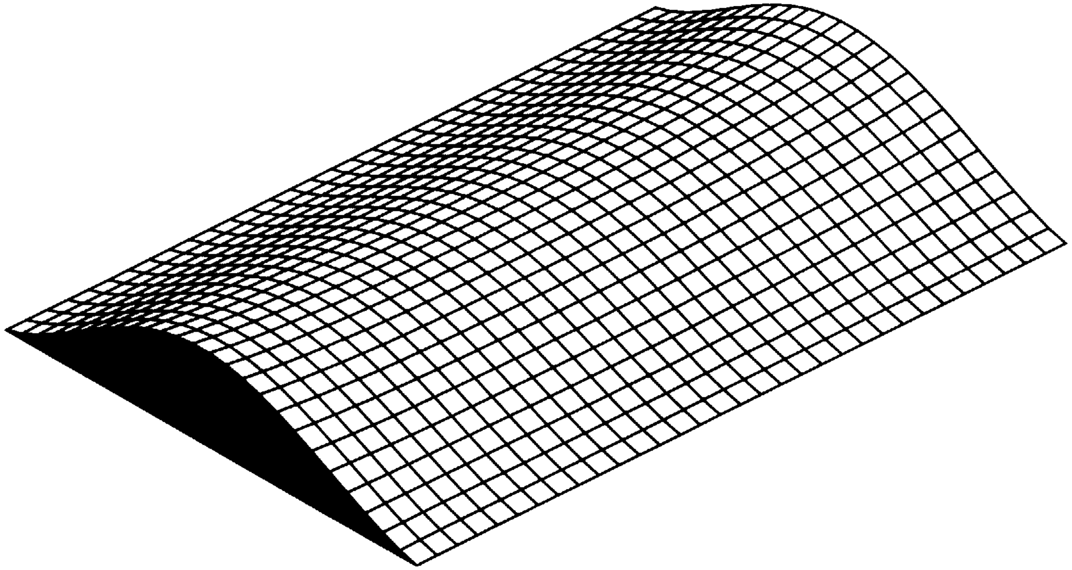

Figure 6. First mode for Al plate.

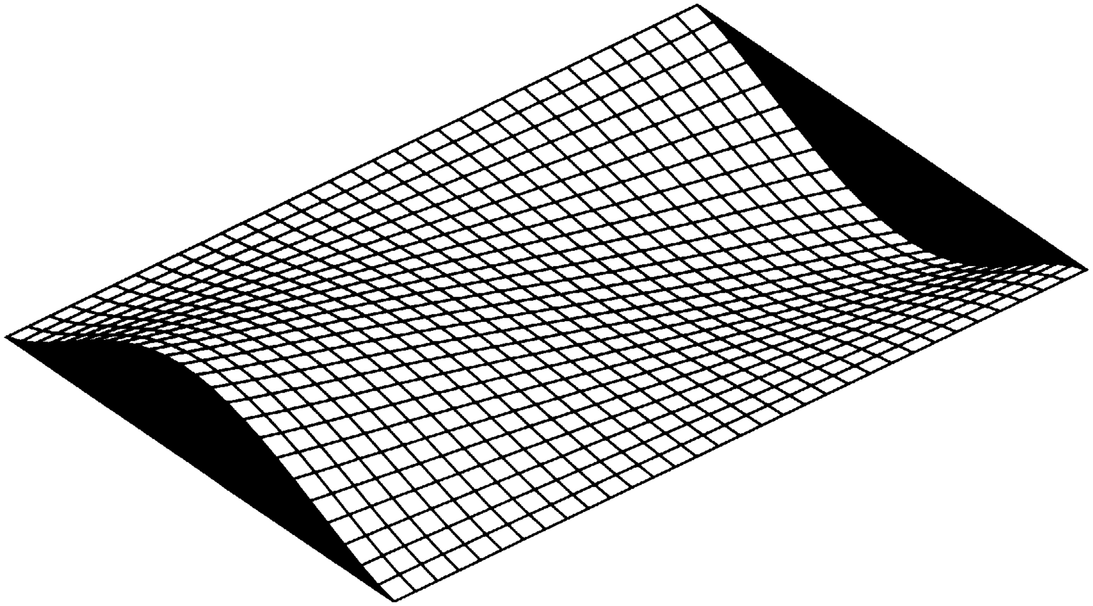

Figure 7. Second mode for Al plate.

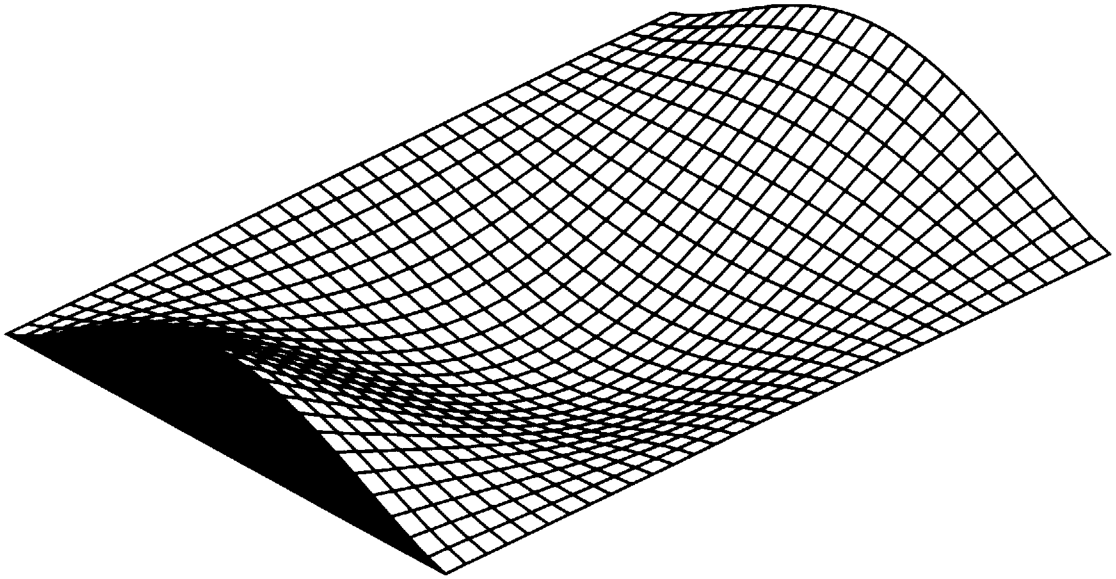

Figure 8. Third mode for Al plate.

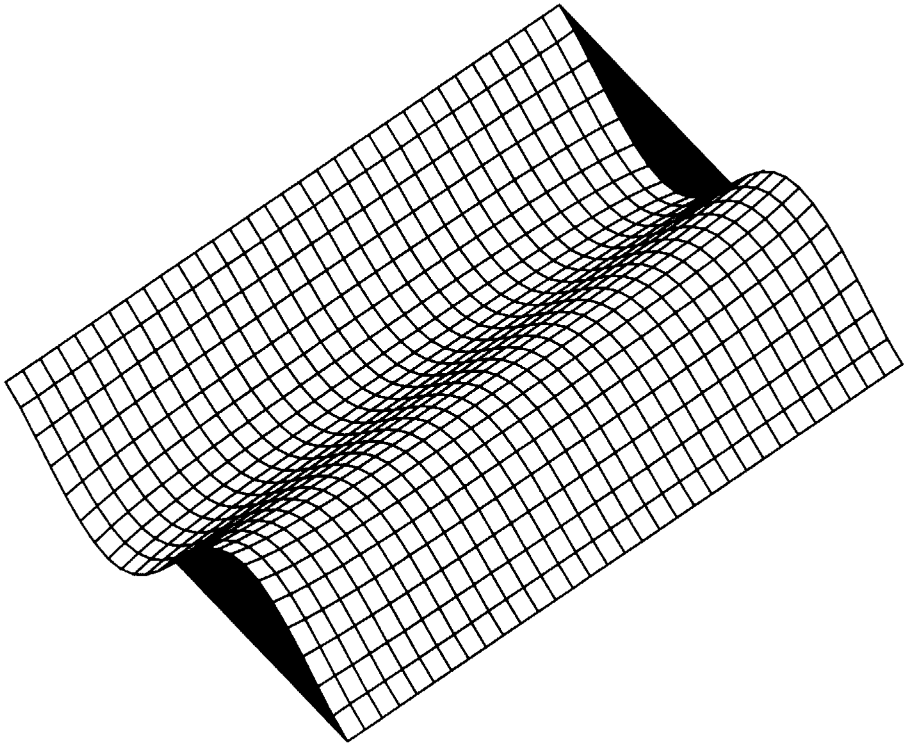

Figure 9. Fourth mode for Al plate.

Stacking Sequence $[(0\pm60)_2]_s$			
Layer	Angle	Ply Thickness (in)	
1	N/A	.002	Al
2	N/A	.003	Adhesive
3	0	.005	Ply 1
4	60	.005	Ply 2
5	-60	.005	Ply 3
6	0	.005	Ply 4
7	60	.005	Ply 5
8	-60	.005	Ply 6
9	-60	.005	Ply 7
10	60	.005	Ply 8
11	0	.005	Ply 9
12	-60	.005	Ply 10
13	60	.005	Ply 11
14	0	.005	Ply 12
15	N/A	.003	Adhesive
16	N/A	.002	Al

Figure 10. Stacking sequence for the composite heat sink.

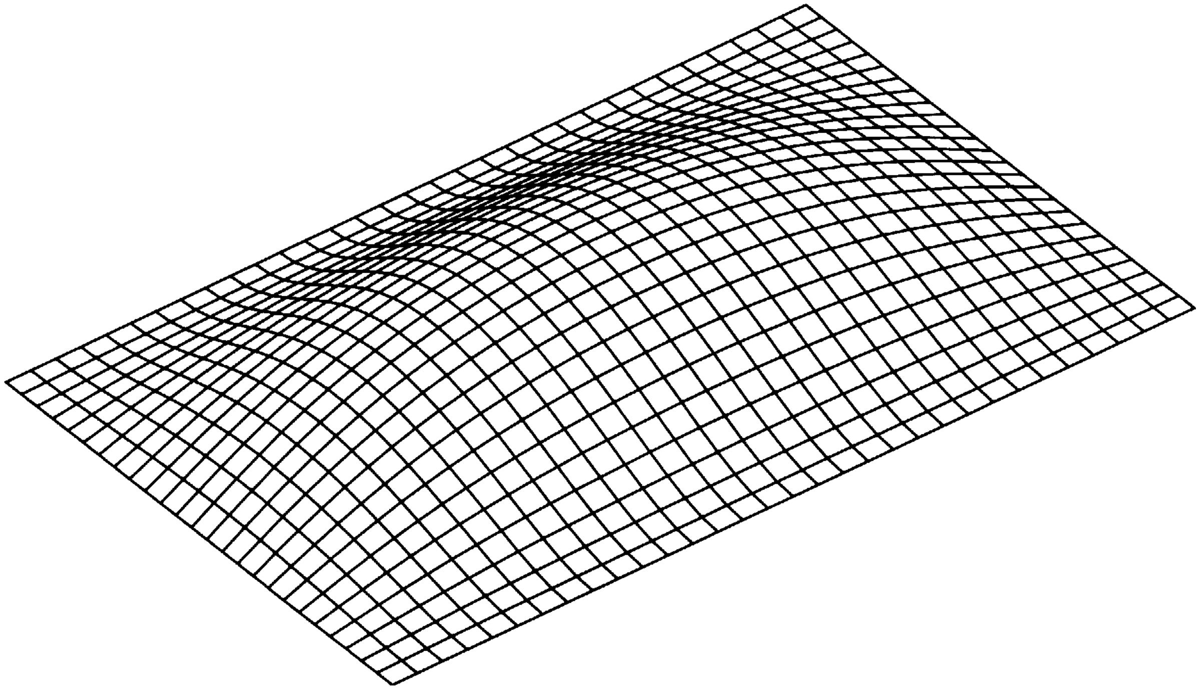

Figure 11. Plate displacement under a uniform load.

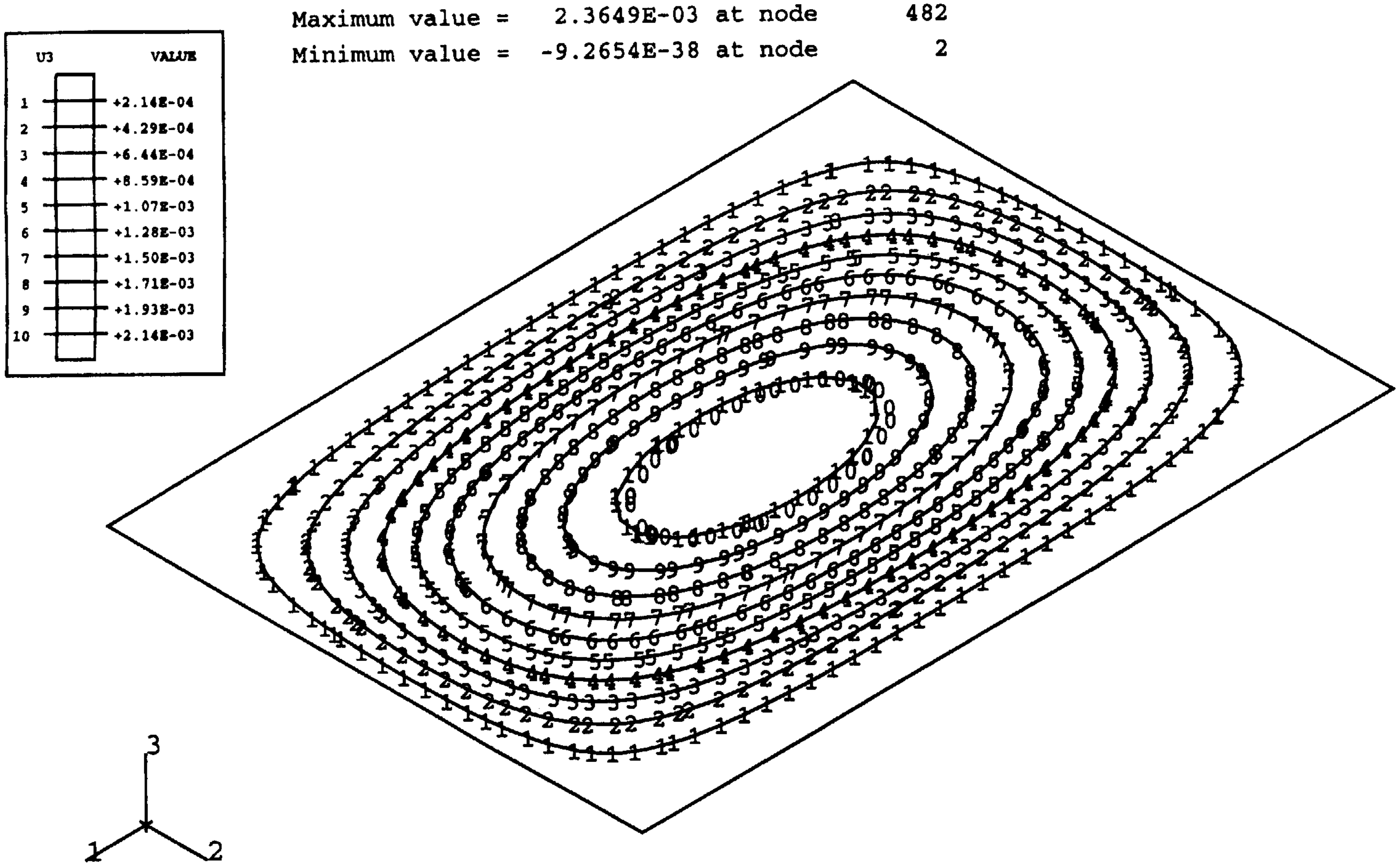

Figure 12. Composite heat sink deflection under a uniform load.

[0°] fiber orientation:

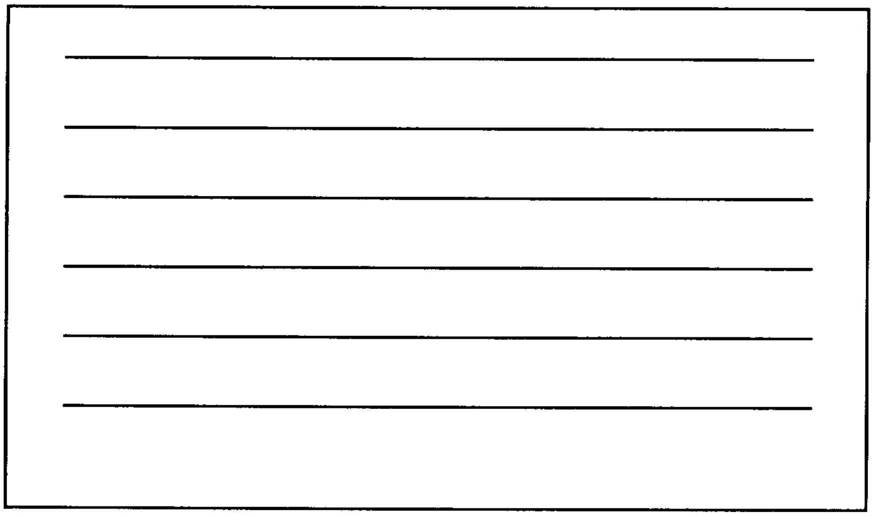

[90°] fiber orientation:

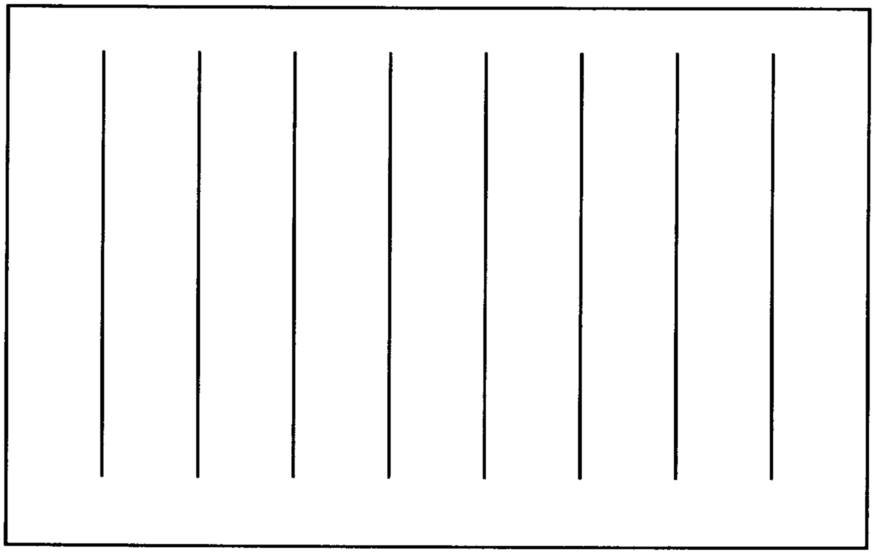

Figure 13. Switching fiber orientation for altering stiffness (not to scale).

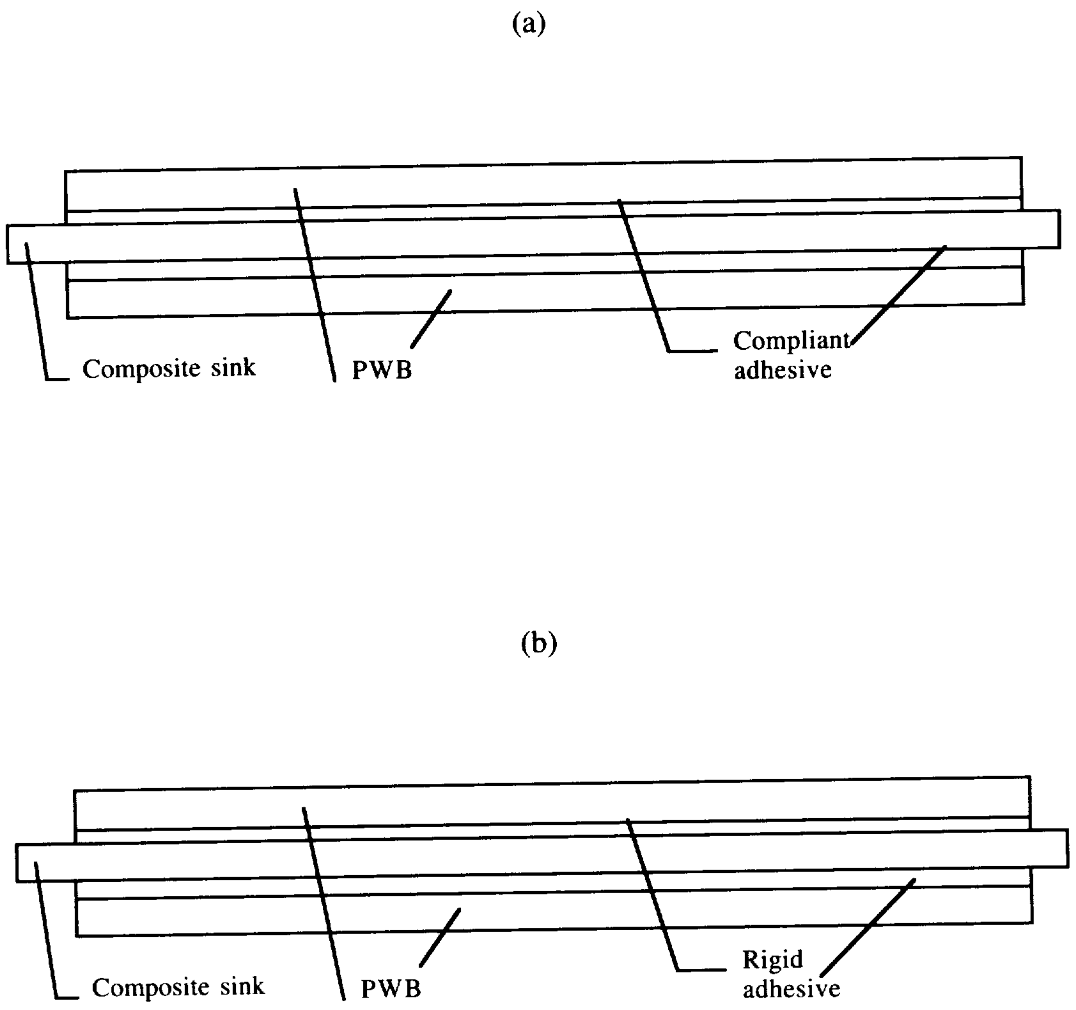

Figure 14a and b. PWB assemblies using different adhesives for heat sink attachment (not to scale).

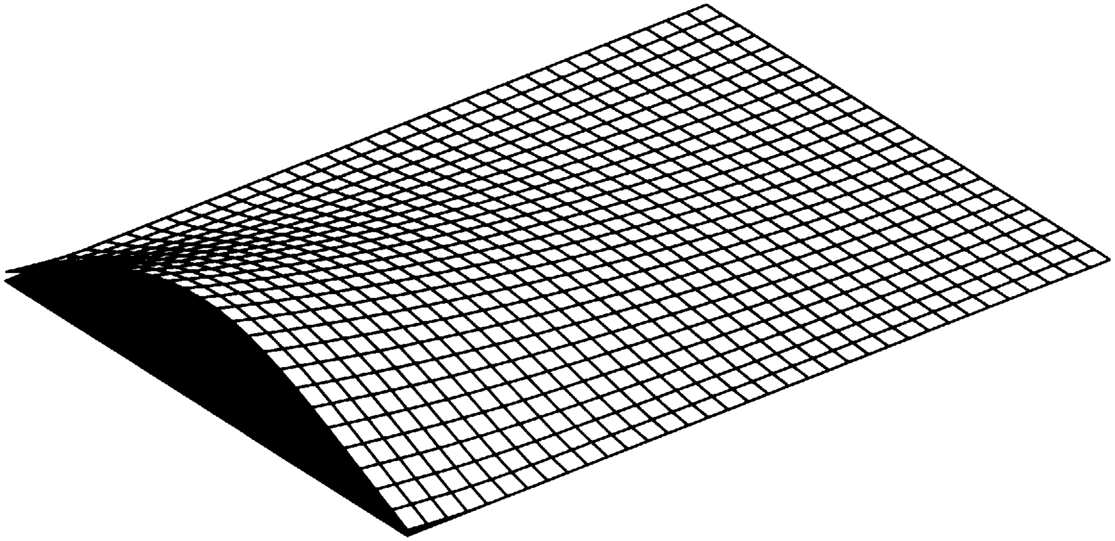

Figure 15. First mode for PWB assembly with composite heat sink.

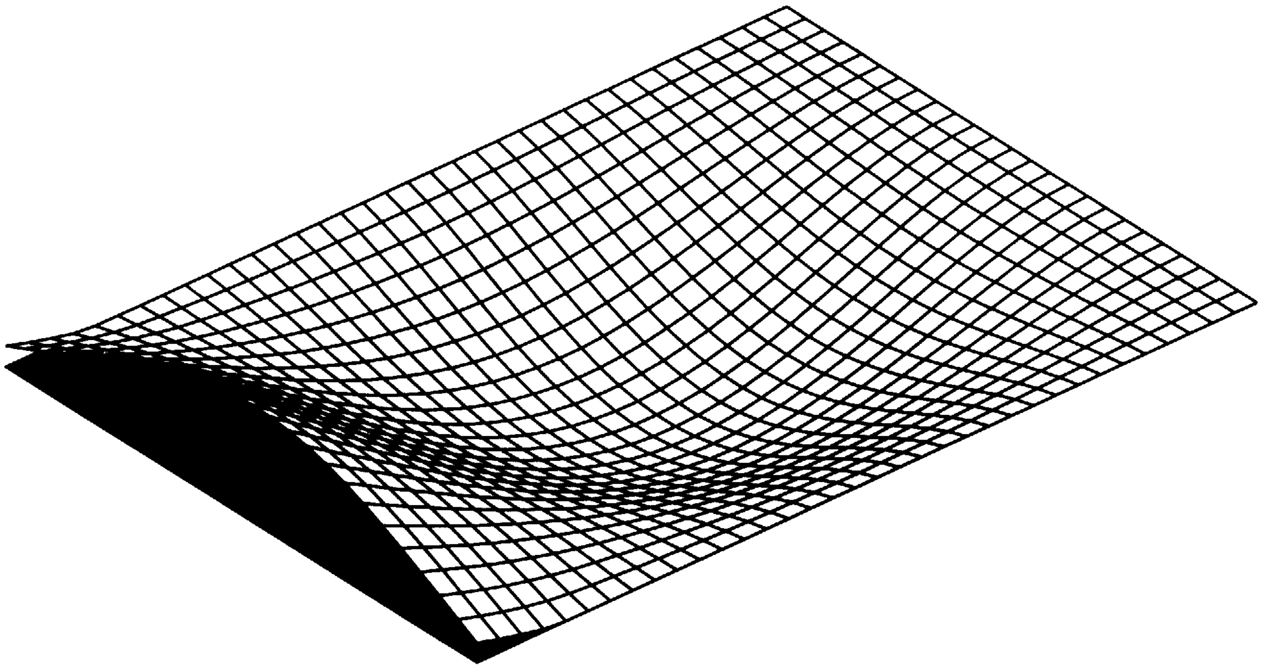

Figure 16. Second mode for PWB assembly with composite heat sink.

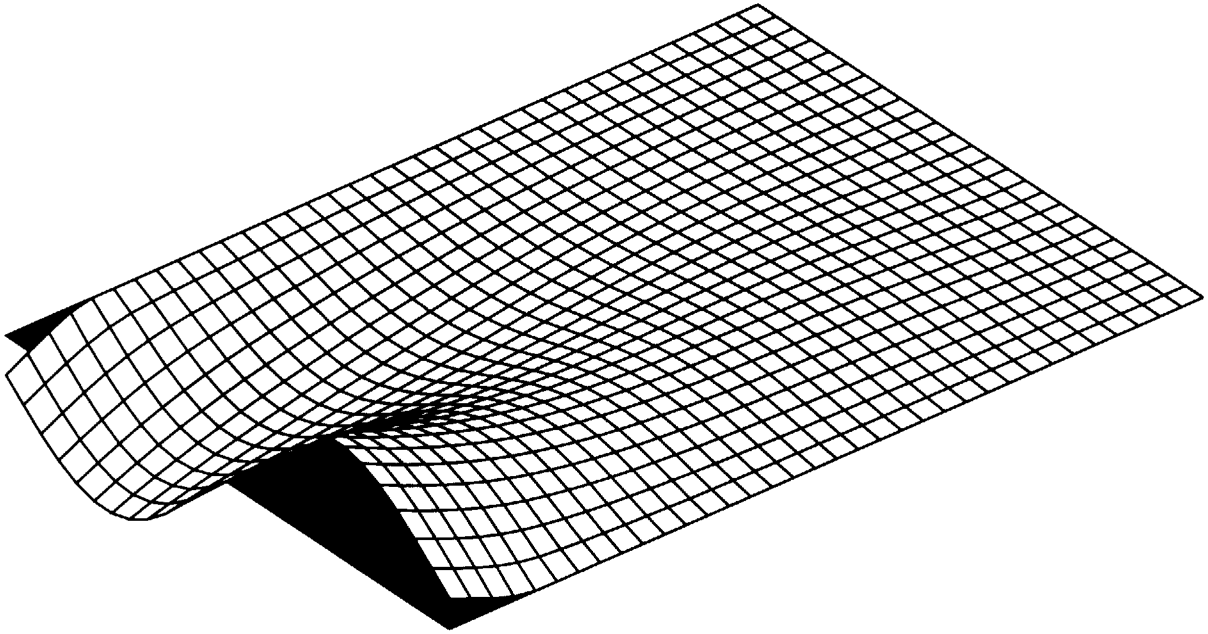

Figure 17. Third mode for PWB assembly with composite heat sink.

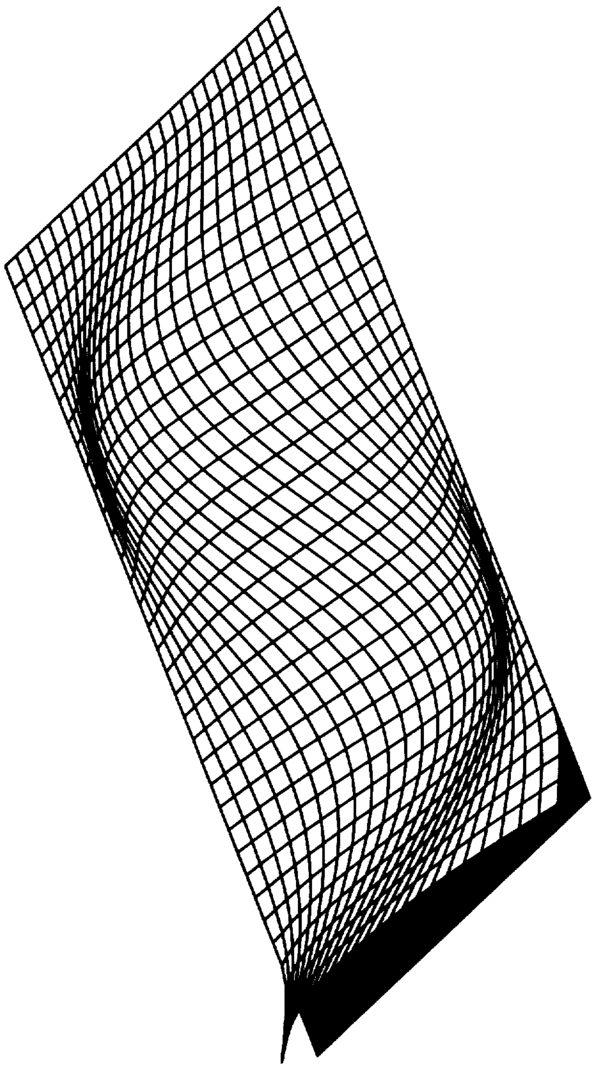

Figure 18. Fourth mode for PWB assembly with composite heat sink.

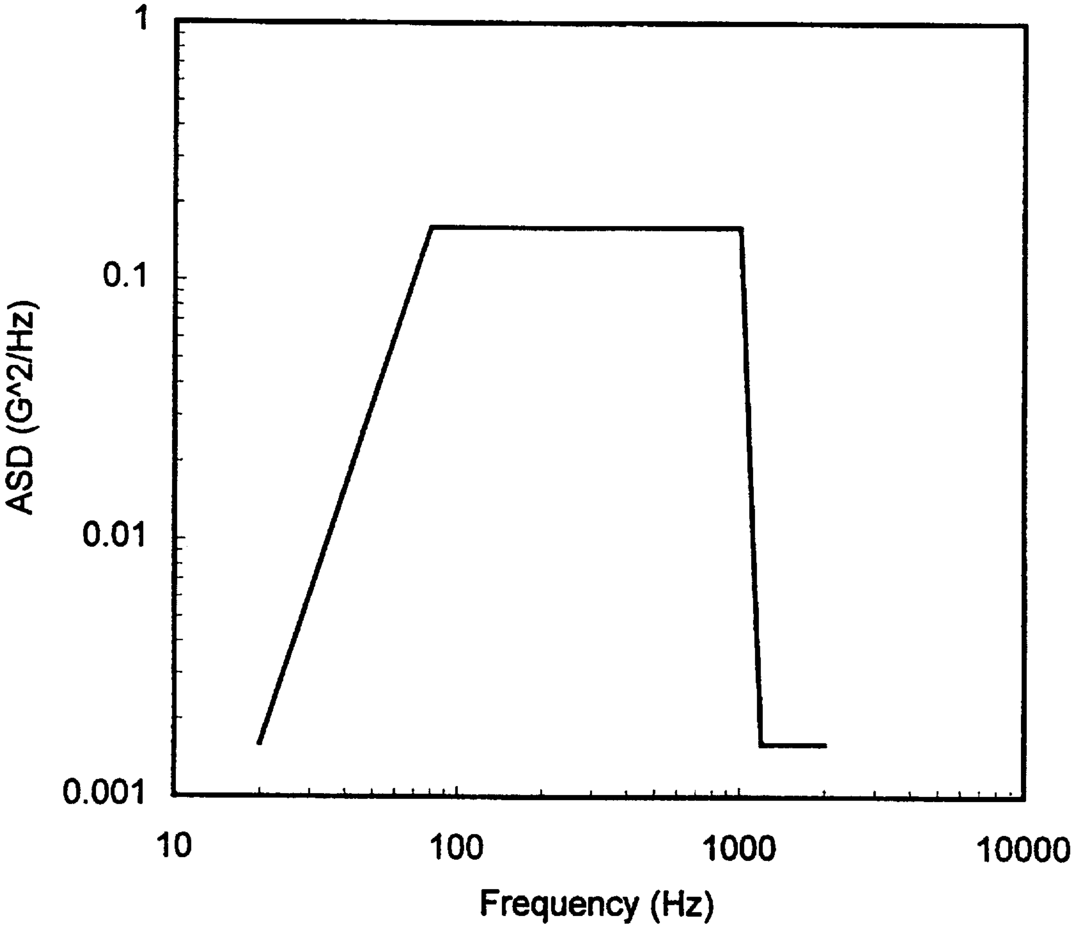

Figure 19. ASD for random vibration analysis.

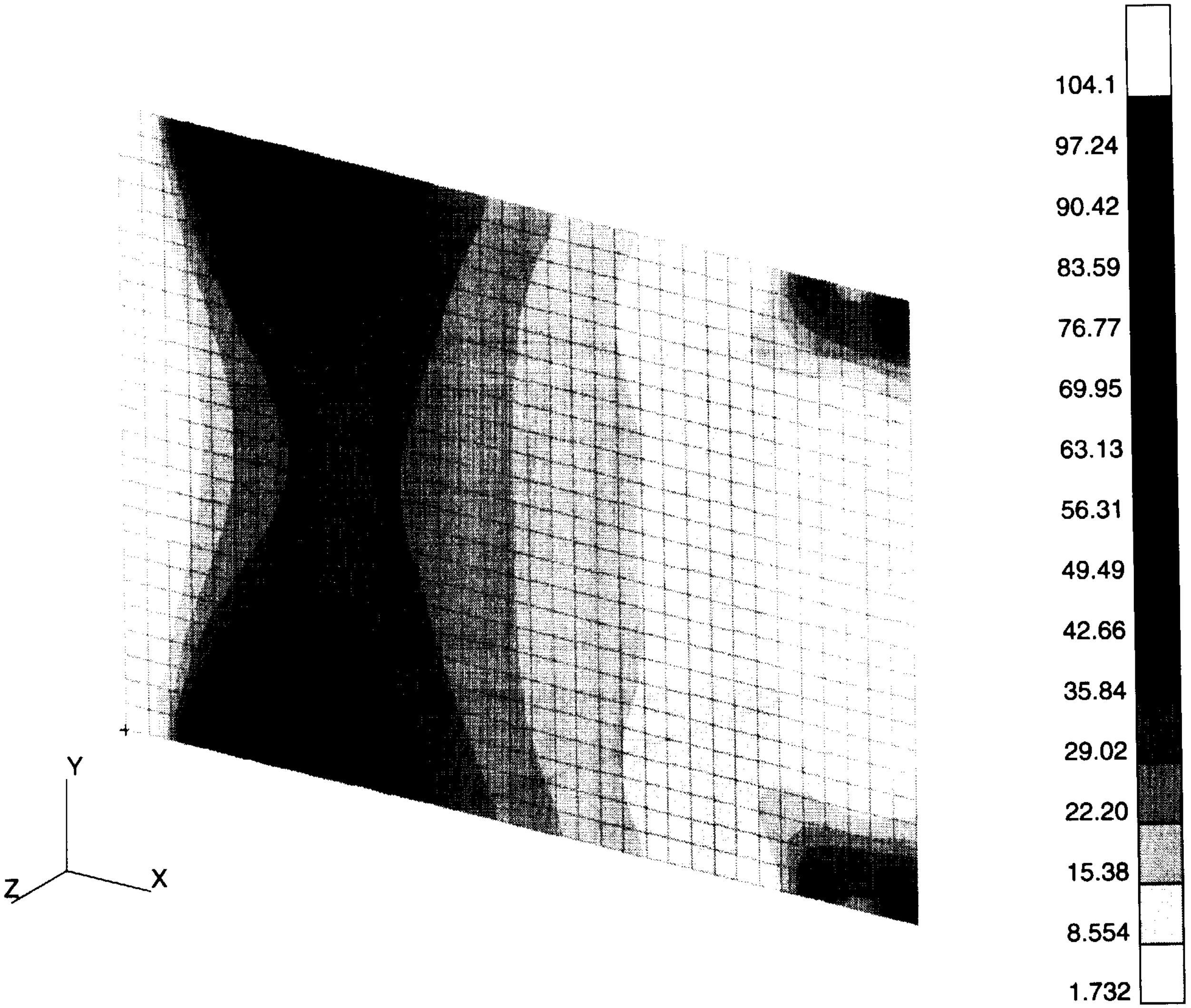

Figure 20. Maximum shear stress in the rigid adhesive layer.

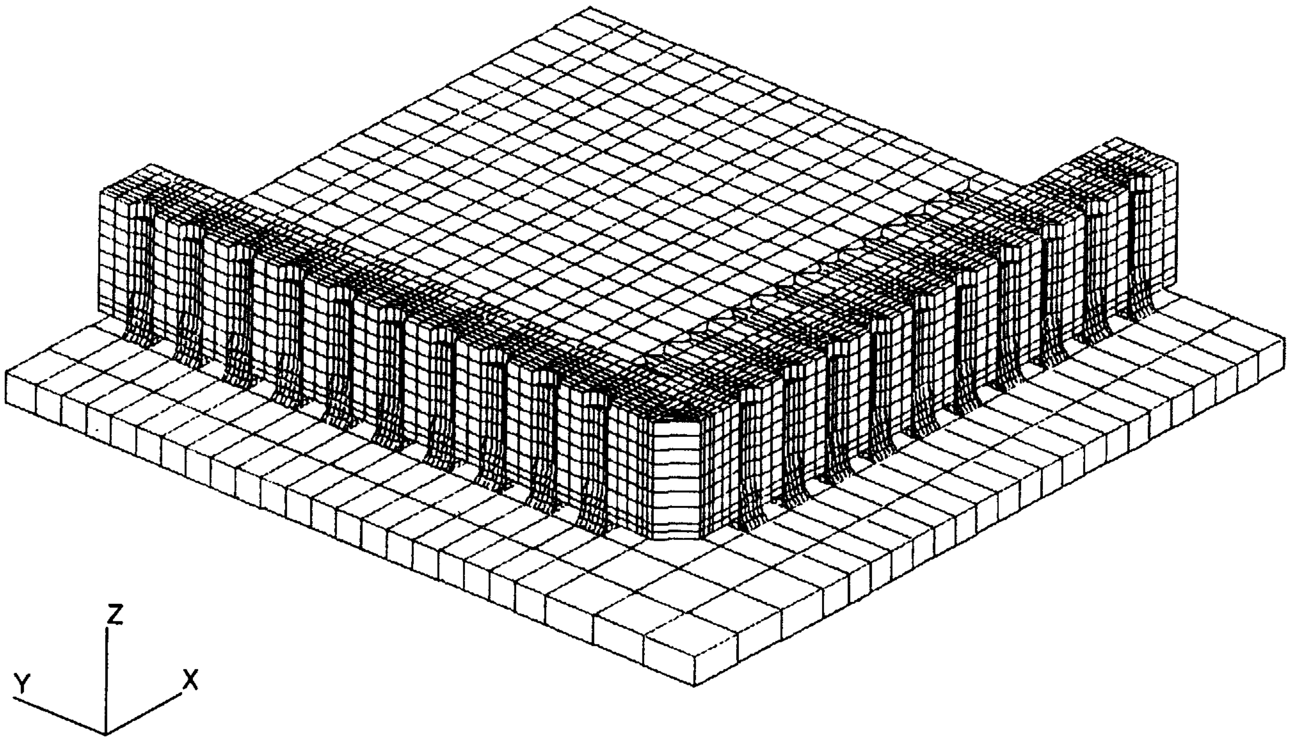

Figure 21. 1/4 FEA model for the largest LCC.

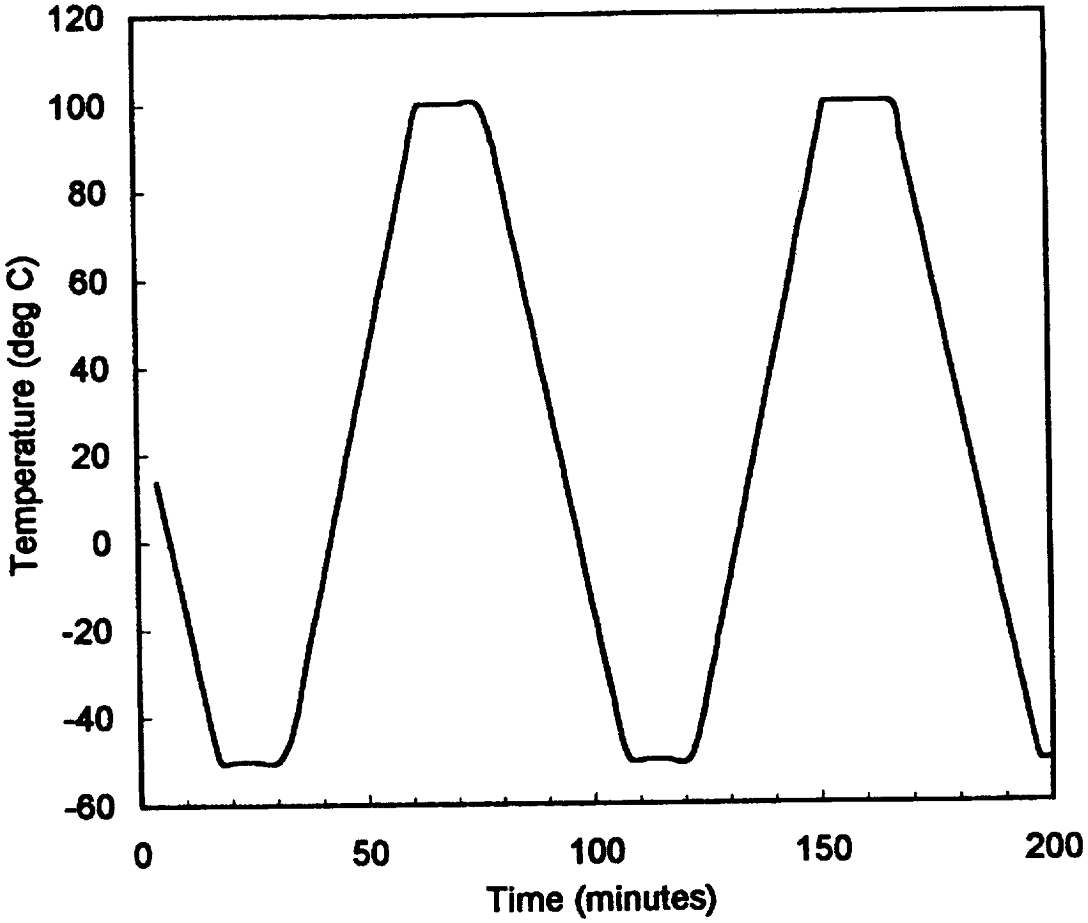

Figure 22. Temperature cycling profile.

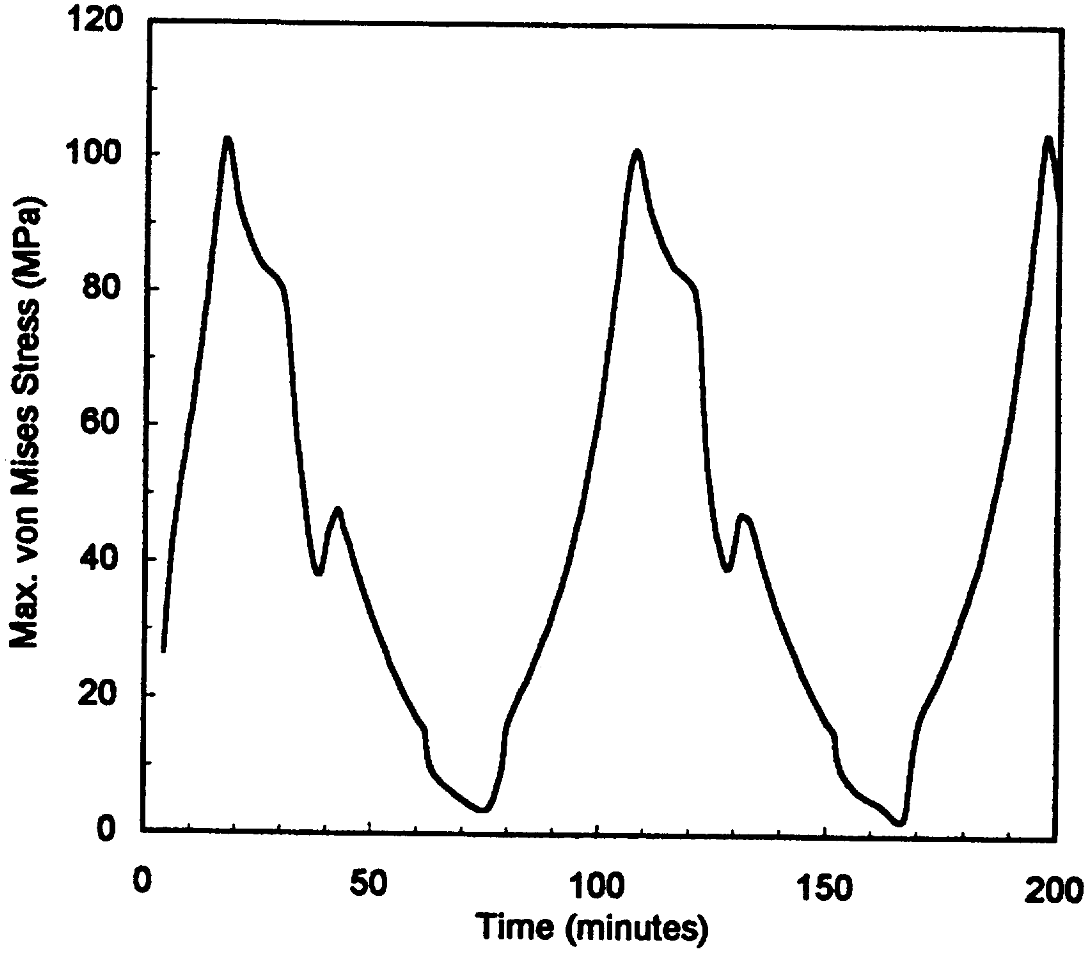

Figure 23. Maximum local von Mises stress in ther corner solder joint.

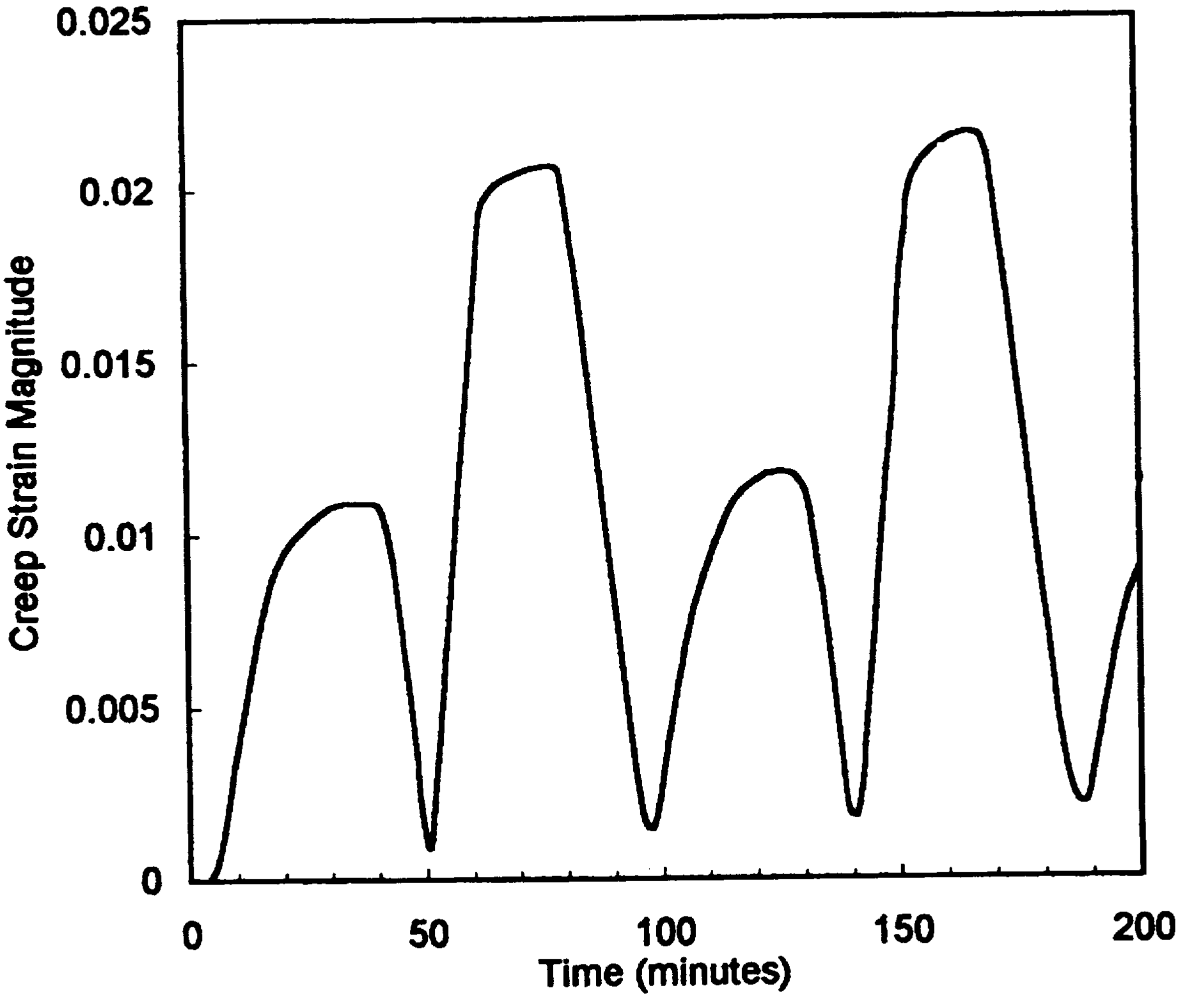

Figure 24. Creep strain magniture in the corner solder joint.

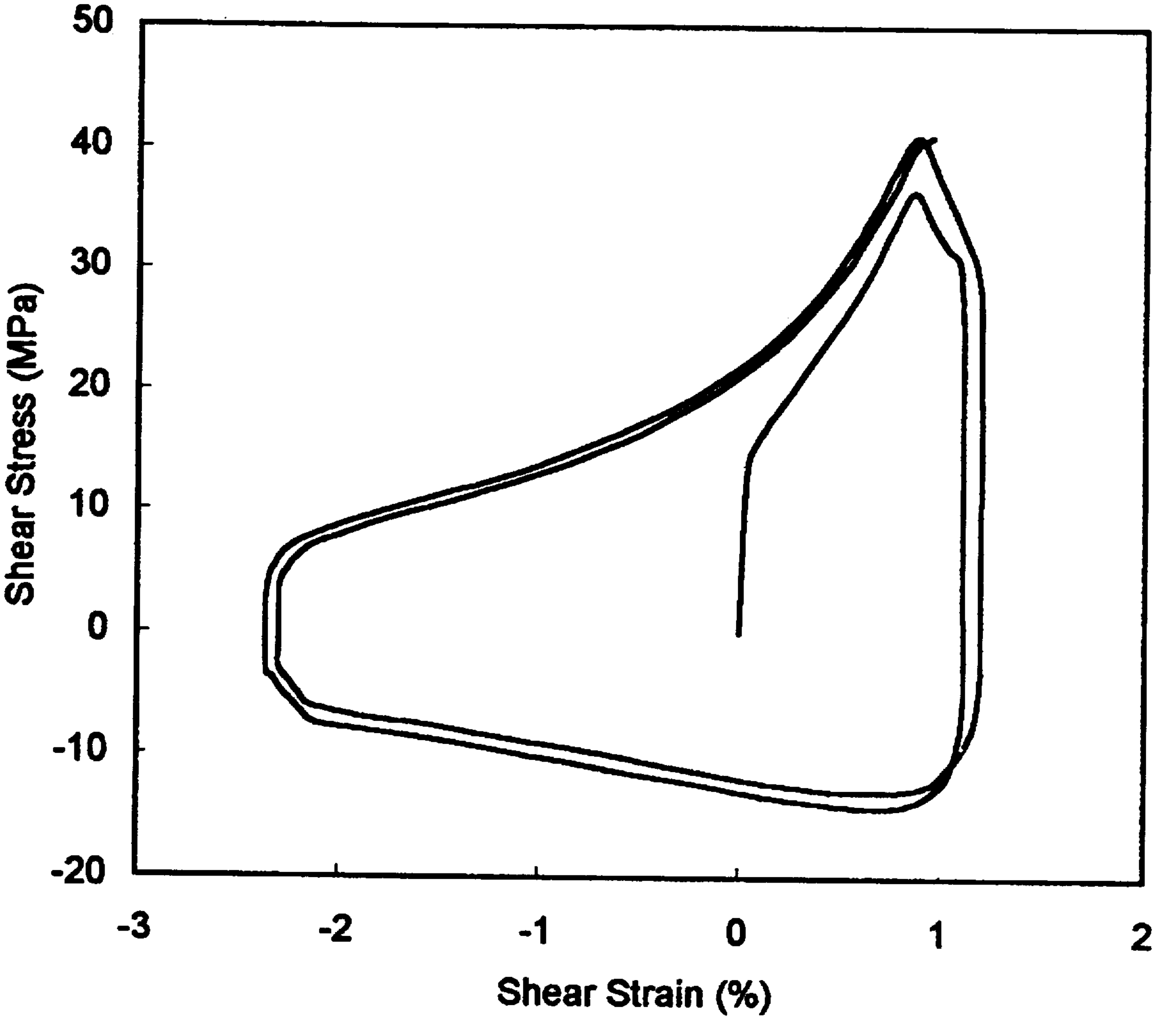

Figure 25. Hysteresis loop showing creep ratcheting phenomenon.

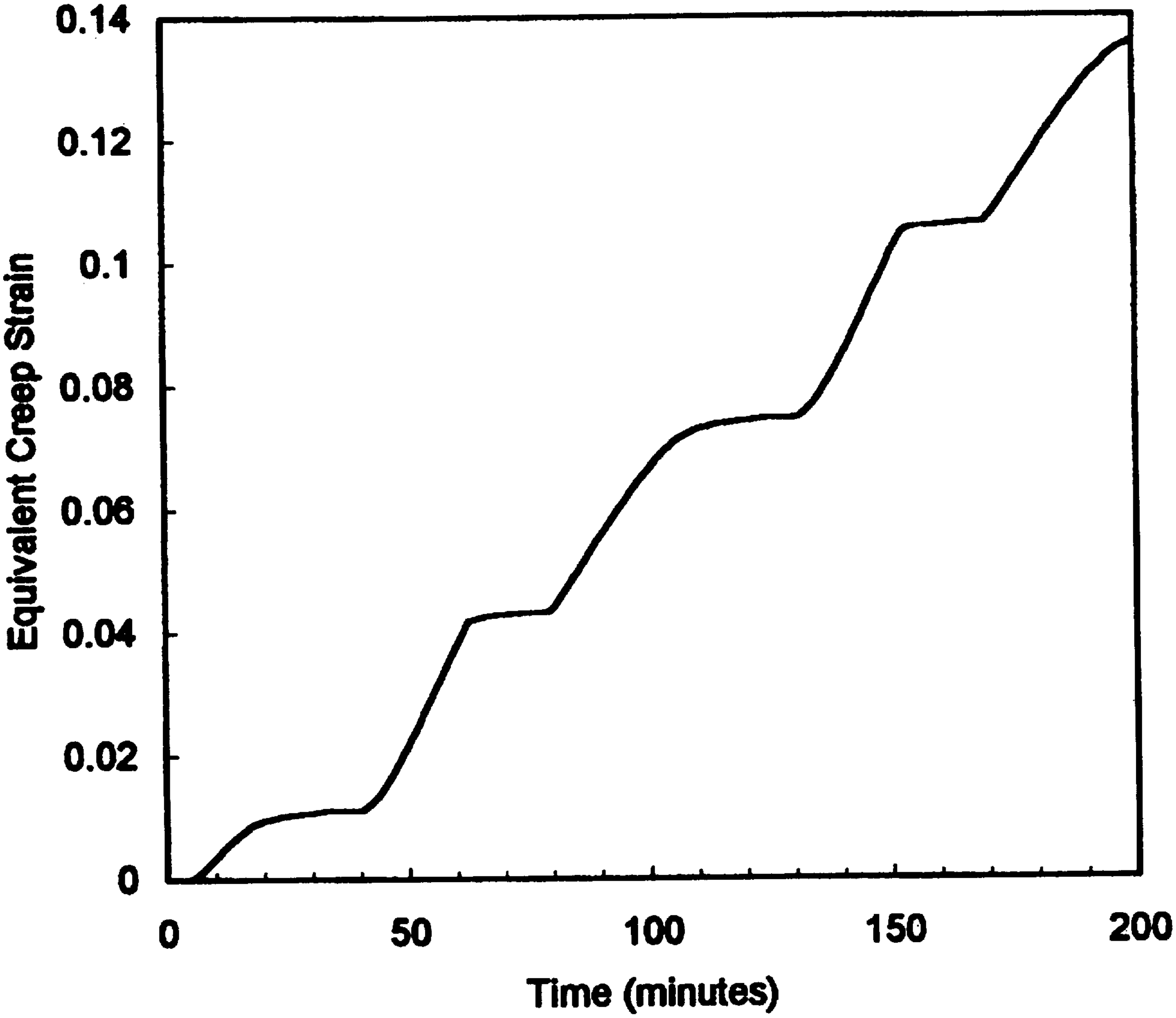

Figure 26. Equivalent creep strain in the corner solder joint.

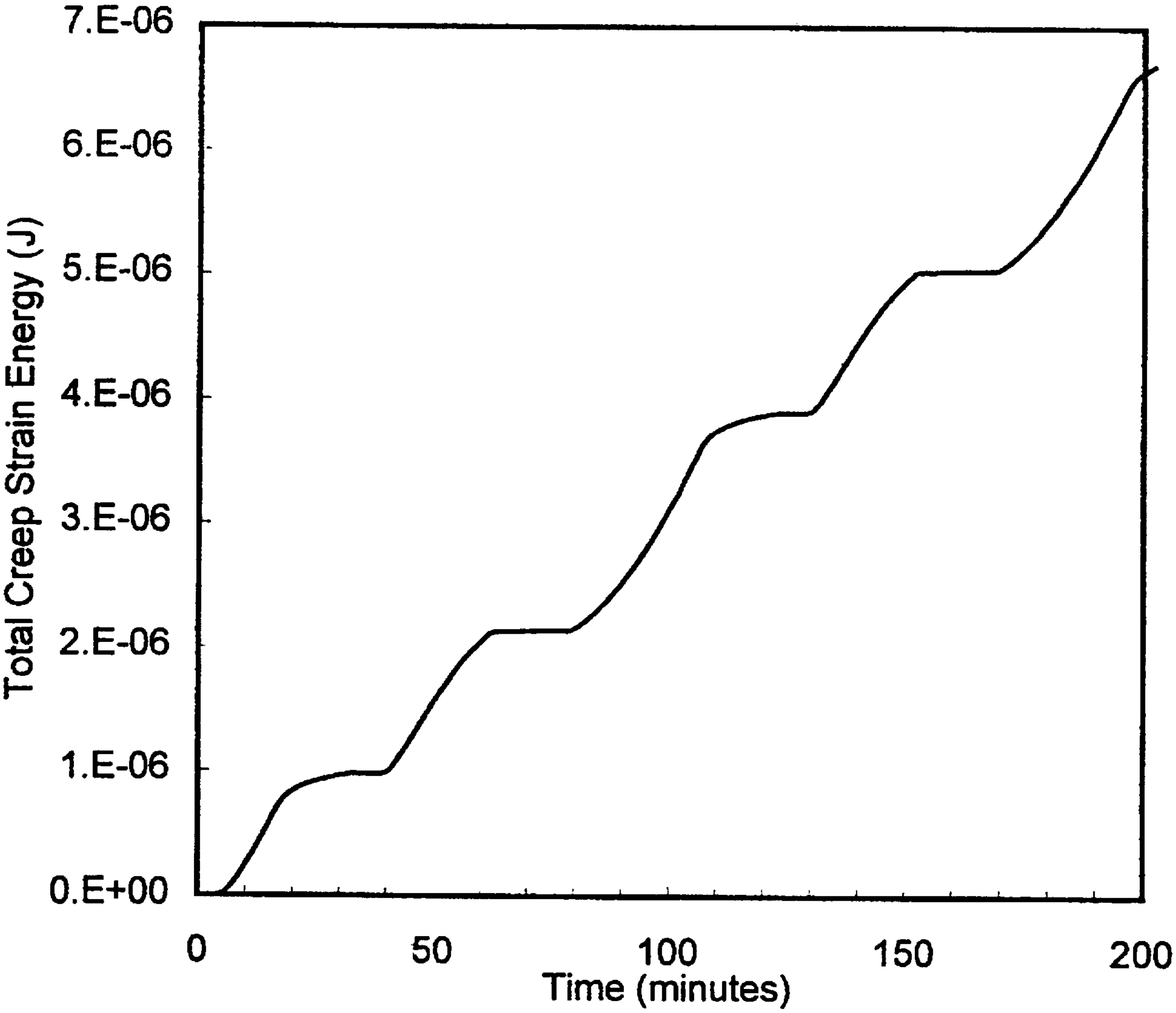

Figure 27. Total creep strain energy in the corner solder joint.

APPENDIXES

1. Weight Reduction Comparison
2. Matrices of Lamina for $[(0\pm60)_2]_s$ Stacking Sequence

Appendix 1. Weight Reduction Comparison

Table A1

	Composite Heat Sink	Aluminum Heat Sink
Al Skin Volume (in^3)	10.53×7.528×0.004	N/A
Adhesive Volume (in^3)	10.53×7.528×0.006	N/A
Sink Core Volume (in^3)	10.53×7.528×0.060	10.53×7.528×0.080
Total Weight (lb)	0.335	0.621
Weight Reduction	46%	-

Appendix 2. Matrices of Lamina for $[(0\pm60)_2]_s$ Stacking Sequence

(1) Stress-strain relation (Msi):

$$\begin{Bmatrix}\varepsilon_{11}\\ \varepsilon_{22}\\ \gamma_{12}\end{Bmatrix}=\begin{pmatrix}S_{11} & S_{12} & 0\\ S_{21} & S_{22} & 0\\ 0 & 0 & S_{66}\end{pmatrix}\begin{Bmatrix}\sigma_{11}\\ \sigma_{22}\\ \tau_{12}\end{Bmatrix}=\begin{pmatrix}\dfrac{1}{E_{11}} & -\dfrac{\nu_{12}}{E_{11}} & 0\\ -\dfrac{\nu_{21}}{E_{22}} & \dfrac{1}{E_{22}} & 0\\ 0 & 0 & \dfrac{1}{G_{12}}\end{pmatrix}\begin{Bmatrix}\sigma_{11}\\ \sigma_{22}\\ \tau_{12}\end{Bmatrix}$$

$$=\begin{pmatrix}0.014 & -0.0047 & 0\\ -0.0047 & 1.43 & 0\\ 0 & 0 & 1.35\end{pmatrix}\begin{Bmatrix}\sigma_{11}\\ \sigma_{22}\\ \tau_{12}\end{Bmatrix} \qquad \text{(A2-1)}$$

(2) Lamina stiffness matrix (Msi):

$$\begin{Bmatrix}\sigma_{11}\\ \sigma_{22}\\ \tau_{12}\end{Bmatrix}=\begin{pmatrix}Q_{11} & Q_{12} & 0\\ Q_{21} & Q_{22} & 0\\ 0 & 0 & 2Q_{66}\end{pmatrix}\begin{Bmatrix}\varepsilon_{11}\\ \varepsilon_{22}\\ \gamma_{12}/2\end{Bmatrix}=\begin{pmatrix}\dfrac{E_{11}}{1-\nu_{12}\nu_{21}} & \dfrac{\nu_{12}E_{22}}{1-\nu_{12}\nu_{21}} & 0\\ \dfrac{\nu_{12}E_{22}}{1-\nu_{12}\nu_{21}} & \dfrac{E_{22}}{1-\nu_{12}\nu_{21}} & 0\\ 0 & 0 & 2G_{12}\end{pmatrix}\begin{Bmatrix}\varepsilon_{11}\\ \varepsilon_{22}\\ \gamma_{12}/2\end{Bmatrix}$$

$$=\begin{pmatrix}68.31 & 0.22 & 0\\ 0.22 & 0.70 & 0\\ 0 & 0 & 1.48\end{pmatrix}\begin{Bmatrix}\varepsilon_{11}\\ \varepsilon_{22}\\ \gamma_{12}/2\end{Bmatrix} \qquad \text{(A2-2)}$$

(3) Transformed lamina stiffness matrix for +60° ply (Msi):

The following transformation relations are used:

$$
\begin{aligned}
Q_{11}^{T} &= Q_{11}\cos^4\theta + Q_{22}\sin^4\theta + 2(Q_{12} + 2Q_{66})\sin^2\theta\cos^2\theta \\
Q_{12}^{T} &= (Q_{11} + Q_{22} - 4Q_{66})\sin^2\theta\cos^2\theta + Q_{12}(\sin^4\theta + \cos^4\theta) \\
Q_{22}^{T} &= Q_{11}\sin^4\theta + Q_{22}\cos^4\theta + 2(Q_{12} + 2Q_{66})\sin^2\theta\cos^2\theta \\
Q_{16}^{T} &= (Q_{11} - Q_{12} - 2Q_{66})\cos^3\theta\sin\theta - (Q_{22} - Q_{12} - 2Q_{66})\sin^3\theta\cos\theta \\
Q_{26}^{T} &= (Q_{11} - Q_{12} - 2Q_{66})\cos\theta\sin^3\theta - (Q_{22} - Q_{12} - 2Q_{66})\sin\theta\cos^3\theta \\
Q_{66}^{T} &= (Q_{11} + Q_{22} - 2Q_{12} - 2Q_{66})\sin^2\theta\cos^2\theta + Q_{66}(\sin^4\theta + \cos^4\theta)
\end{aligned}
\tag{A2-3}
$$

$$
[Q]_{+60} = \begin{pmatrix} 5.3 & 12.52 & 7.53 \\ 12.52 & 39.10 & 21.73 \\ 7.53 & 21.73 & 13.03 \end{pmatrix}
$$

(4) Transformed lamina stiffness matrix for -60° ply (Msi):

$$
[Q]_{-60} = \begin{pmatrix} 5.3 & 12.52 & -7.53 \\ 12.52 & 39.10 & -21.73 \\ -7.53 & -21.73 & 13.03 \end{pmatrix}
$$

REPORT DOCUMENTATION PAGE	Form Approved OMB No. 0704-0188

1. AGENCY USE ONLY *(Leave blank)*	**2. REPORT DATE** May 1997	**3. REPORT TYPE AND DATES COVERED** Technical Paper

4. TITLE AND SUBTITLE Structural Design and Analysis of a Light-Weight Laminated Composite Heat Sink for Spaceflight PWBs	**5. FUNDING NUMBERS** Code 310
6. AUTHOR(S) Mark S. Fan and W. Lee Niemeyer	
7. PERFORMING ORGANIZATION NAME(S) AND ADDRESS (ES) Goddard Space Flight Center Greenbelt, Maryland 20771	**8. PEFORMING ORGANIZATION REPORT NUMBER** 97B00050
9. SPONSORING / MONITORING AGENCY NAME(S) AND ADDRESS (ES) National Aeronautics and Space Administration Washington, DC 20546-0001	**10. SPONSORING / MONITORING AGENCY REPORT NUMBER** NASA TP-3679

11. SUPPLEMENTARY NOTES

Fan: NASATechnology Validation Assurance Program, Greenbelt, Maryland
Niemeyer: Goddard Space Flight Center, Greenbelt, Maryland

12a. DISTRIBUTION / AVAILABILITY STATEMENT Unclassified - Unlimited Subject Category 33 Availability: NASA CASI (301) 621-0390.	**12b. DISTRIBUTION CODE**

13. ABSTRACT *(Maximum 200 words)*

In order to reduce the overall weight in spaceborne electronic systems, a conventional metallic heat sink typically used for double-sided printed wiring boards was suggested to be replaced by light-weight and high-strength laminated composite materials. Through technology validation assurance (TVA) approach, it has been successfully demonstrated that using laminated composite heat sink can not only reduce the weight of the heat sink by nearly 50%, but also significantly lower the internal thermally-induced stresses that are largely responsible for potential delamination under cyclic temperature variations. With composite heat sink, both thermal and dynamic performance of the double-sided printed wiring board (PWB) exceeds that of its counterpart with metallic heat sink. Also included in this work is the original contribution to the understanding of creep behavior of the worst-case leadless chip carrier (LCC) surface mount solder joint. This was identified as the interconnection most susceptible to thermal fatigue damage in the PWB assembly.

14. SUBJECT TERMS PWB; Wedge lock; Natural frequency; Laminated composite; Thermal stress; Random vibration; Creep; Fatigue; Creep strain.	**15. NUMBER OF PAGES** 68
	16. PRICE CODE

17. SECURITY CLASSIFICATION OF REPORT Unclassified	**18. SECURITY CLASSIFICATION OF THIS PAGE** Unclassified	**19. SECURITY CLASSIFICATION OF ABSTRACT** Unclassified	**20. LIMITATION OF ABSTRACT** UL